

## BICEP2 I: DETECTION OF $B$ -mode POLARIZATION AT DEGREE ANGULAR SCALES

BICEP2 COLLABORATION - P. A. R. ADE<sup>1</sup>, R. W. AIKIN<sup>2</sup>, D. BARKATS<sup>3</sup>, S. J. BENTON<sup>4</sup>, C. A. BISCHOFF<sup>5</sup>, J. J. BOCK<sup>2,6</sup>, J. A. BREVIK<sup>2</sup>, I. BUDER<sup>5</sup>, E. BULLOCK<sup>7</sup>, C. D. DOWELL<sup>6</sup>, L. DUBAND<sup>8</sup>, J. P. FILIPPINI<sup>2</sup>, S. FLIESCHER<sup>9</sup>, S. R. GOLWALA<sup>2</sup>, M. HALPERN<sup>10</sup>, M. HASSELFIELD<sup>10</sup>, S. R. HILDEBRANDT<sup>2,6</sup>, G. C. HILTON<sup>11</sup>, V. V. HRISTOV<sup>2</sup>, K. D. IRWIN<sup>12,13,11</sup>, K. S. KARKARE<sup>5</sup>, J. P. KAUFMAN<sup>14</sup>, B. G. KEATING<sup>14</sup>, S. A. KERNASOVSKIY<sup>12</sup>, J. M. KOVAC<sup>5,17</sup>, C. L. KUO<sup>12,13</sup>, E. M. LEITCH<sup>15</sup>, M. LUEKER<sup>2</sup>, P. MASON<sup>2</sup>, C. B. NETTERFIELD<sup>4,16</sup>, H. T. NGUYEN<sup>6</sup>, R. O'BRIENT<sup>6</sup>, R. W. OGBURN IV<sup>12,13</sup>, A. ORLANDO<sup>14</sup>, C. PRYKE<sup>9,7,17</sup>, C. D. REINTSEMA<sup>11</sup>, S. RICHTER<sup>5</sup>, R. SCHWARZ<sup>9</sup>, C. D. SHEEHY<sup>9,15</sup>, Z. K. STANISZEWSKI<sup>2,6</sup>, R. V. SUDIWALA<sup>1</sup>, G. P. TEPLY<sup>2</sup>, J. E. TOLAN<sup>12</sup>, A. D. TURNER<sup>6</sup>, A. G. VIIEG<sup>5,15</sup>, C. L. WONG<sup>5</sup>, AND K. W. YOON<sup>12,13</sup>

*to be submitted to a journal TBD*

### ABSTRACT

We report results from the BICEP2 experiment, a Cosmic Microwave Background (CMB) polarimeter specifically designed to search for the signal of inflationary gravitational waves in the  $B$ -mode power spectrum around  $\ell \sim 80$ . The telescope comprised a 26 cm aperture all-cold refracting optical system equipped with a focal plane of 512 antenna coupled transition edge sensor (TES) 150 GHz bolometers each with temperature sensitivity of  $\approx 300 \mu\text{K}_{\text{CMB}}\sqrt{\text{s}}$ . BICEP2 observed from the South Pole for three seasons from 2010 to 2012. A low-foreground region of sky with an effective area of 380 square degrees was observed to a depth of 87 nK-degrees in Stokes  $Q$  and  $U$ . In this paper we describe the observations, data reduction, maps, simulations and results. We find an excess of  $B$ -mode power over the base lensed- $\Lambda$ CDM expectation in the range  $30 < \ell < 150$ , inconsistent with the null hypothesis at a significance of  $> 5\sigma$ . Through jackknife tests and simulations based on detailed calibration measurements we show that systematic contamination is much smaller than the observed excess. We also estimate potential foreground signals and find that available models predict these to be considerably smaller than the observed signal. These foreground models possess no significant cross-correlation with our maps. Additionally, cross-correlating BICEP2 against 100 GHz maps from the BICEP1 experiment, the excess signal is confirmed with  $3\sigma$  significance and its spectral index is found to be consistent with that of the CMB, disfavoring synchrotron or dust at  $2.3\sigma$  and  $2.2\sigma$ , respectively. The observed  $B$ -mode power spectrum is well-fit by a lensed- $\Lambda$ CDM + tensor theoretical model with tensor/scalar ratio  $r = 0.20^{+0.07}_{-0.05}$ , with  $r = 0$  disfavored at  $7.0\sigma$ . Subtracting the best available estimate for foreground dust modifies the likelihood slightly so that  $r = 0$  is disfavored at  $5.9\sigma$ .

*Subject headings:* cosmic background radiation — cosmology: observations — gravitational waves — inflation — polarization

### 1. INTRODUCTION

The discovery of the Cosmic Microwave Background (CMB) by Penzias & Wilson (1965) confirmed the hot big bang paradigm and established the CMB as a central tool for the study of cosmology. In recent years, observations of its temperature anisotropies have helped establish and refine the “standard” cosmological model now known as  $\Lambda$ CDM, under which our universe is understood to be spatially flat, dominated by cold dark matter, and with a cosmological constant ( $\Lambda$ ) driving accelerated expansion at late times. CMB temperature measurements have now reached remarkable precision over angular scales ranging from the whole sky to arcminute resolution, producing results in striking concordance with predictions of  $\Lambda$ CDM and constraining its key parameters to sub-percent precision (e.g. Bennett et al. 2013; Hinshaw et al. 2013; Story et al. 2013; Hou et al. 2014; Sievers et al. 2013; Das et al. 2013; Planck Collaboration XV 2013; Planck Collaboration XVI 2013).

Inflationary cosmology extends the standard model by postulating an early period of nearly exponential expansion which sets the initial conditions for the subsequent hot big bang. It was proposed and developed in the early 1980s to resolve mysteries for which the standard model offered no solution, including the flatness, horizon, smoothness, entropy, and monopole problems (Brout et al. 1978; Starobinsky 1980; Kazanas 1980; Sato 1981; Guth 1981; Linde 1982, 1983; Albrecht & Steinhardt 1982; see Planck Collaboration XXII 2013 for a review). Inflation also explains the universe’s

<sup>1</sup> School of Physics and Astronomy, Cardiff University, Cardiff, CF24 3AA, UK

<sup>2</sup> Department of Physics, California Institute of Technology, Pasadena, CA 91125, USA

<sup>3</sup> Joint ALMA Observatory, ESO, Santiago, Chile

<sup>4</sup> Department of Physics, University of Toronto, Toronto, ON, Canada

<sup>5</sup> Harvard-Smithsonian Center for Astrophysics, 60 Garden Street MS 42, Cambridge, MA 02138, USA

<sup>6</sup> Jet Propulsion Laboratory, Pasadena, CA 91109, USA

<sup>7</sup> Minnesota Institute for Astrophysics, University of Minnesota, Minneapolis, MN 55455, USA

<sup>8</sup> SBT, Commissariat à l’Energie Atomique, Grenoble, France

<sup>9</sup> Department of Physics, University of Minnesota, Minneapolis, MN 55455, USA

<sup>10</sup> Department of Physics and Astronomy, University of British Columbia, Vancouver, BC, Canada

<sup>11</sup> National Institute of Standards and Technology, Boulder, CO 80305, USA

<sup>12</sup> Department of Physics, Stanford University, Stanford, CA 94305, USA

<sup>13</sup> Kavli Institute for Particle Astrophysics and Cosmology, SLAC National Accelerator Laboratory, 2575 Sand Hill Rd, Menlo Park, CA 94025, USA

<sup>14</sup> Department of Physics, University of California at San Diego, La Jolla, CA 92093, USA

<sup>15</sup> University of Chicago, Chicago, IL 60637, USA

<sup>16</sup> Canadian Institute for Advanced Research, Toronto, ON, Canada

<sup>17</sup> Corresponding authors: pryke@physics.umn.edu and jmkovac@cfa.harvard.edu

primordial perturbations as originating in quantum fluctuations stretched by this exponential expansion (Mukhanov & Chibisov 1981; Hawking 1982; Guth & Pi 1982; Starobinsky 1982; Bardeen et al. 1983; Mukhanov 1985), and thus to be correlated on superhorizon scales. The simplest models further predict these perturbations to be highly adiabatic and Gaussian and nearly scale-invariant (though typically slightly stronger on larger scales). These qualities, though not necessarily unique to the inflationary paradigm, have all been confirmed by subsequent observations (e.g., Spergel & Zaldarriaga 1997; Peiris et al. 2003, and references above). Although highly successful, the inflationary paradigm represents a vast extrapolation from well-tested regimes in physics. It invokes quantum effects in highly curved spacetime at energies near  $10^{16}$  GeV and timescales less than  $10^{-32}$  s. A definitive test of this paradigm would be of fundamental importance.

Gravitational waves generated by inflation have the potential to provide such a definitive test. Inflation predicts that the quantization of the gravitational field coupled to exponential expansion produces a primordial background of stochastic gravitational waves with a characteristic spectral shape (Grishchuk 1975; Starobinsky 1979; Rubakov et al. 1982; Fabri & Pollock 1983; Abbott & Wise 1984; also see Krauss & Wilczek 2013). Though unlikely to be directly detectable in modern instruments, these gravitational waves would have imprinted a unique signature upon the CMB. Gravitational waves induce local quadrupole anisotropies in the radiation field within the last-scattering surface, inducing polarization in the scattered light (Polnarev 1985). This polarization pattern will include a “curl” or  $B$ -mode component at degree angular scales that cannot be generated primordially by density perturbations. The amplitude of this signal depends upon the tensor-to-scalar ratio,  $r$ , which itself is a function of the energy scale of inflation. The detection of  $B$ -mode polarization of the CMB at large angular scales would provide a unique confirmation of inflation and a probe of its energy scale (Seljak 1997; Kamionkowski et al. 1997; Seljak & Zaldarriaga 1997).

The CMB is polarized with an amplitude of a few  $\mu\text{K}$ , dominated by the “gradient” or  $E$ -mode pattern that is generated by density perturbations at last scattering. These  $E$ -modes peak at angular scales of  $\sim 0.2^\circ$ , corresponding to angular multipole  $\ell \approx 1000$ . They were first detected by the DASI experiment (Kovac et al. 2002). Since then multiple experiments have refined measurements of the  $EE$  power spectrum, including CAPMAP (Barkats et al. 2005; Bischoff et al. 2008), CBI (Readhead et al. 2004; Sievers et al. 2007), BOOMERANG03 (Montroy et al. 2006), WMAP (Page et al. 2007; Bennett et al. 2013), MAXIPOL (Wu et al. 2007), QUAD (Pryke et al. 2009; Brown et al. 2009), BICEP1 (Chiang et al. 2010; Barkats et al. 2014), and QUIET (QUIET Collaboration et al. 2011, 2012).

Gravitational lensing of the CMB’s light by large scale structure at relatively late times produces small deflections of the primordial pattern, converting a small portion of  $E$ -mode power into  $B$ -modes. The lensing  $B$ -mode spectrum is similar to a smoothed version of the  $E$ -mode spectrum but a factor  $\sim 100$  lower in power, and hence also rises toward sub-degree scales and peaks around  $\ell \approx 1000$ . The inflationary gravitational wave (IGW)  $B$ -mode, however, is predicted to peak at multipole  $\ell \approx 80$  and this creates an opportunity to search for it around this scale where it is quite distinct from the lensing

effect.<sup>18</sup>

A large number of current CMB experimental efforts now target  $B$ -mode polarization. Evidence for lensing  $B$ -mode polarization at sub-degree scales has already been detected by two experiments in the past year, first by the SPT telescope (Hanson et al. 2013) and more recently by POLARBEAR (POLARBEAR Collaboration et al. 2013a,b, 2014). The search for inflationary  $B$ -modes at larger scales will also be a goal of these experiments, as well as other ongoing experimental efforts in the US that include the ABS (Hileman et al. 2009), ACTPOL (Niemack et al. 2010), and CLASS (Eimer et al. 2012) ground-based telescopes and the EBEX (Reichborn-Kjennerud et al. 2010), SPIDER (Fraisse et al. 2013), and PIPER (Kogut et al. 2012) balloon experiments, each employing a variety of complementary strategies. It is also a major science goal of the ESA *Planck* satellite mission.

The BICEP/Keck Array series of experiments have been specifically designed to search for primordial  $B$ -mode polarization on degree angular scales by making very deep maps of relatively small patches of sky from the South Pole. The BICEP1 instrument initiated this series (Keating et al. 2003), observing from 2006 to 2008. Its initial results were described in Takahashi et al. (2010) and Chiang et al. (2010) (hereafter T10 and C10), and final results were recently reported in Barkats et al. (2014) (hereafter B14) yielding a limit of  $r < 0.70$  at 95% confidence.

In this paper we report results from BICEP2 — a successor to BICEP1 which differed principally in the focal plane where a very large increase in the detector count resulted in more than an order of magnitude improvement in mapping speed. The observation field and strategy were largely unchanged, as were the telescope mount, observation site etc. Using all three seasons of data taken with BICEP2 (2010–2012) we detect  $B$ -mode power in the multipole range  $30 < \ell < 150$ , finding this power to have a strong excess inconsistent with lensed  $\Lambda\text{CDM}$  at  $> 5\sigma$  significance.

The structure of this paper is as follows. In §2 and §3 we briefly review the BICEP2 instrument, observations and low-level data reduction deferring details to a companion paper BICEP2 Collaboration II (2014) (hereafter the Instrument Paper). In §4 we describe our map making procedure and present signal and signal-differenced “jackknife”  $T$ ,  $Q$  and  $U$  maps which have unprecedented sensitivity. This section introduces “deprojection” of modes potentially contaminated through beam systematics which is an important new technique. In §5 we describe our detailed timestream-level simulations of signal and pseudo-simulations of noise. In §6 we describe calculation of the power spectra, including matrix-based  $B$ -mode purification. In §7 we present the signal and jackknife power spectrum results for  $TE$ ,  $EE$ ,  $BB$ ,  $TB$  and  $EB$ . In §8 we discuss and summarize the many studies we have conducted probing for actual and potential sources of systematic contamination, and argue that residual contamination is much smaller than the detected  $B$ -mode signal. Full details are deferred to a companion paper BICEP2 Collaboration III (2014) (hereafter the Systematics Paper). In §9 we investigate foreground projections based on external data and conclude that it is implausible that the  $B$ -mode signal which we see is dominated by dust, synchrotron or any other known

<sup>18</sup>This is the so-called “recombination bump”. There is another opportunity to search for the IGW signal at  $\ell < 10$  in the “reionization bump” but this requires observations over a substantial fraction of the full sky.

foreground source. In §10 we take cross spectra of the BICEP2 maps with those from BICEP1 (as presented in B14) and find that the spectral signature of the signal is consistent with the CMB. Finally in §11 we calculate some simple, largely phenomenological, parameter constraints, and conclude in §12.

## 2. THE BICEP2 INSTRUMENT

BICEP2 was similar to BICEP1 (see T10) reusing the same telescope mount and installation at the South Pole. Like BICEP1 the optical system was a simple 26 cm aperture all-cold refractor housed entirely in a liquid helium cooled cryostat. The main differences from BICEP1 were the use of a focal plane array of planar antenna-coupled devices (Bock 2003) with voltage-biased transition-edge sensor (TES) detectors (Irwin 1995) and a multiplexed superconducting quantum interference device (SQUID) readout. BICEP2 observed at 150 GHz only. A very brief review of the instrument follows — for more details please refer to the Instrument Paper.

### 2.1. Optics

The optics were adapted from the original BICEP1 design (Keating et al. 2003). Light entered the cryostat through a polypropylene foam window, passed through PTFE filters cooled to 100 K and 40 K, and then through polyethylene objective and eyepiece lenses cooled to 4 K. A 26.4 cm diameter aperture stop was placed at the objective lens and an additional nylon filter was placed on the sky side of the eyepiece lens. All the lenses and filters were antireflection coated and the interior of the optics tube was lined with microwave absorber. The optics were designed to be telecentric (flat focal plane) and the resulting beams had full-width-half-max of  $\approx 0.5^\circ$ . An absorptive forebaffle was mounted on the front of the telescope which was designed to prevent radiation from boresight angles greater than  $\sim 20^\circ$  entering the telescope. The telescope was located inside a large stationary reflective groundscreen.

### 2.2. Focal Plane

The BICEP2 focal plane employed monolithic arrays of antenna coupled TES detectors designed and fabricated at Caltech/JPL. Each pixel was composed of two interleaved  $12 \times 12$  arrays of orthogonal slot antennas feeding beam-forming (phased-array) summing trees. The output of each summing tree was a microstrip which passed through a band-defining filter and deposited its power on a thermally isolated island. Changes in the power incident on this island were detected using a transition edge sensor (TES). There was an  $8 \times 8$  array of pixels on each tile, and four such tiles were combined to form the complete focal plane unit. There were thus, in principle, 256 dual-polarization pixels in the focal plane for a total of 512 detectors, each with temperature sensitivity of  $\approx 300 \mu\text{K}_{\text{CMB}}/\sqrt{\text{s}}$ . (Six pixels were deliberately disconnected between antenna and TES sensor to provide diagnostic “dark” channels.) The focal plane was cooled to 270 mK by a closed cycle three-stage sorption refrigerator.

### 2.3. Detector Readout and DAQ System

The TES detectors were read out through time-division SQUID multiplexing chips provided by NIST. A single readout channel was connected in rapid succession to 32 detectors, reducing wiring and heat load requirements. These SQUID systems were biased and read out by a Multi-Channel Electronics (MCE) crate external to the cryostat (provided by

UBC). The housekeeping and readout electronics were connected to a set of Linux-based computers running a control system called *gcp*, originally developed for the CBI experiment and developed and reused by many experiments since.

### 2.4. Telescope Mount

The receiver cryostat was mounted on a three-axis mount able to move in azimuth and elevation and to rotate the entire telescope about its boresight. Hereafter we refer to the line-of-sight rotation angle as the “deck” angle. The window of the telescope looked out through an opening in a flexible environmental seal such that the cryostat, mount and electronics were all located in a room temperature laboratory environment.

## 3. OBSERVATIONS AND LOW LEVEL DATA REDUCTION

### 3.1. Observations

BICEP2 observed on a three day schedule locked to sidereal time. As in BICEP1, the basic unit of observation was a  $\approx 50$  minute “scanset” during which the telescope scanned back-and-forth 53 times at  $2.8^\circ \text{ s}^{-1}$  in azimuth in a smooth turnaround triangle wave pattern, with a throw of  $\approx 60^\circ$ , at fixed elevation. We refer to each of the 106 motions across the field (either left- or right-going) as a “half-scan”. We do not use the turnaround portions of the scans in this analysis.

BICEP2 observed the same CMB field as BICEP1 — a low foreground region centered at RA 0h, Dec.  $-57.5^\circ$ . At the South Pole, the elevation angle is simply the negative of declination and azimuth maps to RA shifting by  $15^\circ$  per hour. The scan speed on the sky was thus  $\approx 1.5^\circ \text{ s}^{-1}$  mapping multipole  $\ell = 100$  into the timestream at  $\approx 0.4 \text{ Hz}$ . At the end of each scanset the elevation was stepped by  $0.25^\circ$  and the azimuth angle updated to recenter on RA 0h. The scans thus “slide” with respect to the sky during each scanset by  $\approx 12.5^\circ$  allowing us to subtract a scan fixed “template” from the timestream while leaving degree-scale sky structure only slightly attenuated (see Sections 4.1 and 6.3).

A total of 21 elevation offsets were used between Dec. of  $-55^\circ$  and  $-60^\circ$ . Note that since the field of view of the focal plane —  $\sim 20^\circ$  — is much larger in Dec., and somewhat larger in RA, than the region scanned by the boresight the final coadded map is naturally apodized. After a complete three-day schedule the instrument was rotated to a new deck angle, the refrigerator was re-cycled, and the process repeated. See the Instrument Paper for more details of the observation strategy.

The control system ran CMB observation schedules relentlessly between early 2010 and late 2012 collecting over 17,000 scansets of data ( $\approx 590$  days). (There were some breaks for beam mapping and other calibrations during the austral summers.) The raw data were transferred off-site daily via satellite, allowing rigorous quality monitoring and ongoing analysis development. The analysis presented in this paper uses all of the CMB data taken by BICEP2.

### 3.2. Analysis Pipeline

The analysis pipeline used in this paper is written in the MATLAB language and was originally developed for the QUAD experiment (Pryke et al. 2009). It was then adapted to BICEP1 data and became the secondary, and then primary, analysis pipeline for the C10 and B14 papers, respectively. For BICEP2 it has seen substantial further development including the addition of a sophisticated automatic data selection framework, full deprojection of beam systematics, and

a map-based  $B$ -mode purification operation; these enhancements are detailed below.

### 3.3. Transfer Function Correction and Deglitching

Starting from the raw timestreams, the first step of the pipeline is to deconvolve the temporal response of the instrument. The TES detectors themselves have a very fast and uniform response at all frequencies of interest. To correct for the effect of the digital low-pass filtering, which was applied to the data before it was downsampled for recording to disk, we apply an FIR deconvolution operation in the time domain (which also re-applies a zero-delay low pass filter). Glitches and flux jumps in the SQUID readout are also corrected and/or flagged at this point — they are relatively rare in these data. See the Instrument Paper for more details.

### 3.4. Relative Gain Calibration

At the beginning and end of each scanset an elevation nod or “elnod” was performed. The telescope was moved up/down/up or vice versa in a roughly sinusoidal excursion in time, injecting a signal proportional to the atmospheric opacity gradient into the detector timestreams. In analysis, each elnod is regressed against the airmass profile through which it was looking to derive a relative gain coefficient in SQUID feedback units per airmass. The timestream for each scanset is then divided by its own elnod coefficient and multiplied by the median over all good detectors. This roughly equalizes the gain of each channel and results in considerable cancellation of atmospheric fluctuations when taking the difference of detector pairs, thus making the data considerably easier to work with. The relative gain as determined using the atmospheric gradient is not necessarily the relative gain which minimizes leakage of CMB temperature anisotropy to polarization — see §8. Absolute calibration is deferred until after the final coadded map is made — see §4.8.

### 3.5. First Round Data Cuts

At this point in the data reduction individual channels are cut at per half-scan granularity. Reasons for removal include glitches and flux jumps in the channel in question, or its multiplex neighbors, and synchronization problems in the DAQ system. BICEP2 data are very well behaved and over 90% of the data pass this stage.

## 4. MAP MAKING

### 4.1. Timestream Filtering

In the next step the sum and difference of each detector pair is taken, the pair-sum being ultimately used to form maps of temperature anisotropy, and the pair-difference to measure polarization. Each half-scan is then subjected to a third order polynomial filtering.

Each half-scan is constrained to have the same number of time samples. In addition to the polynomial filtering we also perform a “template” subtraction of any scan-synchronous component by averaging together the corresponding points over a scanset and removing the result from each half-scan. Forward and backward half-scans are treated separately.

Within our simulation-based analysis framework we are free to perform any arbitrary filtering of the data which we choose. Although any given filtering implies some loss of sensitivity due to the removal and mixing of modes within the map these effects are corrected as described in §6.2 and §6.3. We defer discussion of the particular filtering choices made in this analysis to §8.

### 4.2. Pointing Reconstruction

The pointing trajectory of the telescope boresight (i.e. the line of sight axis of rotation of the mount) is determined using a mount pointing model calibrated using a star camera as described in the Instrument Paper. To convert timestream into maps it is then necessary to know the pointing offset of each detector from this direction. To measure these we first make per channel maps assuming approximate offsets, and then regress these against the WMAP5 temperature map to determine corrections. Comparing maps made from left-going and right-going scans at each of the four deck angles, we estimate that this procedure is accurate to better than  $0.05^\circ$  absolute pointing uncertainty. The beam positions relative to the boresight are averaged over the scan directions and deck angles to produce a single reconstruction for each detector used in mapmaking.

### 4.3. Construction of Deprojection Timestream

The two halves of each detector pair would ideally have identical angular response patterns (beams) on the sky. If this is not the case then leakage of temperature anisotropy (pair-sum) to polarization (pair-difference) will occur (Shimon et al. 2008). One can re-sample an external map of the temperature sky and its derivatives to generate templates of the leakage resulting from specific differential beam effects. In this analysis we smooth the *Planck* 143 GHz map<sup>19</sup> using the average measured beam function and resample following the procedure described in Sheehy (2013) and the Systematics Paper. Our standard procedure is to calculate templates for the six modes which correspond to differences of elliptical Gaussian beams. In practice we do not normally use all six — see §4.6 and §8.

### 4.4. Binning into Pairmaps

At this point we bin the pair-sum and pair-difference signals into per-scanset, per-pair RA/Dec. pixel grids which we refer to as “pairmaps”. The pixels are  $0.25^\circ$  square at declination  $-57.5^\circ$ . The data from each scanset are weighted by their inverse variance over the complete scanset (with separate weights for pair-sum and pair-difference). We note that while the pair-sum weights vary widely due to variation in atmospheric  $1/f$  noise, the pair-difference weights are extremely stable over time — i.e. atmospheric fluctuations are empirically shown to be highly unpolarized. For pair-difference a number of products of the timestream and the sine and cosine of the polarization angle are recorded to allow construction of  $Q$  and  $U$  maps as described in §4.7 below. The deprojection templates are also binned into pairmaps in parallel with the pair-difference data.

We use per-pair detector polarization angles derived from a dielectric sheet calibrator (as described in the Instrument Paper)<sup>20</sup>. The measured polarization efficiency of our detectors is very high ( $\approx 99\%$ , see the Instrument Paper) — we perform a small correction to convert temperature-based gains to polarization gains.

### 4.5. Second Round Data Cuts

<sup>19</sup> [http://irsa.ipac.caltech.edu/data/Planck/release\\_1/all-sky-maps/previews/HFI\\_SkyMap\\_143\\_2048\\_R1.10\\_nominal/index.html](http://irsa.ipac.caltech.edu/data/Planck/release_1/all-sky-maps/previews/HFI_SkyMap_143_2048_R1.10_nominal/index.html)

<sup>20</sup> These derived angles are within  $0.2^\circ$  rms of their design values, well within the required accuracy. However note that we later apply an overall rotation to minimize the high  $\ell$   $TB$  and  $EB$  spectra — see §8.2.

The per-scanset, per-pair maps are recorded on disk to allow rapid recalculation of the coadded map while varying the so-called “second round” cut parameters. These include a variety of cuts on the bracketing elnodes, including goodness-of-fit to the atmospheric cosecant model and stability in both absolute and pair-relative senses. We also make some cuts based on the behavior of the data itself including tests for skewness and noise stationarity. Many of these cuts identify periods of exceptionally bad weather and are redundant with one another. We also apply “channel cuts” to remove a small fraction of pairs — principally those with anomalous measured differential beam shapes. In general BICEP2 data are very well-behaved and the final fraction of data retained is 63%. See the Instrument Paper for more details.

#### 4.6. Accumulation of Pairmaps to Phase, and Template Regression

Once the second round cuts have been made we accumulate the pairmaps over each set of ten elevation steps (hereafter referred to as a “phase”). The deprojection templates are also accumulated. We then regress some of these binned templates against the data — i.e. we effectively find the best fit value for each non-ideality, for each pair, within each phase. The templates scaled by the regression coefficients are then subtracted from the data, entirely removing that imperfection mode if present. This operation also filters real signal and noise due to chance correlation (and real  $TE$  induced correlation in the case of signal). This filtering is effectively just additional timestream filtering like that already mentioned in §4.1 and we calibrate and correct for its effect in the same way (see §6.2 and §6.3).

The choice of deprojection timescale is a compromise — reducing it guards against systematic modes which vary over short timescales (as relative gain errors might), while covering more sky before regressing reduces the filtering of real signal (the coefficient is fit to a greater number of pixels). In practice reduction of the filtering going from ten elevation steps to twenty is found to be modest and for this analysis we have deprojected modes on a per-phase basis.

We also have the option to fix the coefficients of any given mode at externally measured values, corresponding to a subtraction of the systematic with no additional filtering of signal. In this analysis we have deprojected differential gain and pointing, and have subtracted the effects of differential ellipticity — we defer discussion of these particular choices to §8.

#### 4.7. Accumulation over Phases and Pairs

We next proceed to coadded maps accumulating over phases and pairs. Full coadds are produced as well as many “jackknife” splits — pairs of maps made from two subsets of the data which might be hypothesized to contain different systematic contamination. Some splits are strictly temporal (e.g. first half vs. second half of the observations), some are strictly pair selections (e.g. inner vs. outer part of each detector tile), and some are both temporal and pair-wise (e.g. the so-called tile/deck jackknife) — see §7.3 for details.

Once the accumulation over all 590 days and  $\approx 200$  detector pairs is done the accumulated quantities must be converted to  $T$ ,  $Q$  and  $U$  maps. For  $T$  this is as simple as dividing by the sum of the weights. For  $Q$  and  $U$  we must perform a simple  $2 \times 2$  matrix inversion for each pixel. This matrix is singular if a given pixel has been observed at only a single value of the deck angle modulo  $90^\circ$ . In general for BICEP2 data we have

angles  $68^\circ$ ,  $113^\circ$ ,  $248^\circ$  and  $293^\circ$  as measured relative to the celestial meridian.

We perform absolute calibration by taking the cross spectrum of the  $T$  map with either the *Planck* 143 GHz map or the WMAP9 W-band  $T$  map as described in the Instrument Paper. We adopt an absolute gain value intermediate to these two measurements and assign calibration uncertainty of 1.3% in the map to account for the difference.

#### 4.8. Maps

Figure 1 shows the BICEP2  $T$ ,  $Q$  and  $U$  signal maps along with a sample set of difference (jackknife) maps. The “vertical-stripe- $Q$ , diagonal-stripe- $U$ ” pattern indicative of an  $E$ -mode dominated sky is visible. Note that these maps are filtered by the relatively large beam of BICEP2 ( $\approx 0.5^\circ$  FWHM). Comparison of the signal and jackknife maps shows that the former are signal dominated — they are the deepest maps of CMB polarization ever made at degree angular scales with an rms noise level of 87 nK in (nominal)  $1^\circ \times 1^\circ$  pixels.

### 5. SIMULATIONS

#### 5.1. Signal Simulations

As is common practice in this type of analysis we account for the filtering which our instrument and data reduction impose on the underlying sky pattern through simulations (Hivon et al. 2002). Starting with input  $T$ ,  $Q$ , and  $U$  maps we smooth using the average measured beam function and then re-sample along the pointing trajectory of each detector at each timestream sample. We have the option of perturbing to per-channel elliptical Gaussian beam shapes using the derivatives of the map (in a similar manner to the construction of the deprojection templates described in §4.3 above). However for our standard simulations we include only differential pointing as this is our leading order beam imperfection (see §8).

We perform three sets of signal-only simulations: i) simulations generated from unlensed  $\Lambda$ CDM input spectra (hereafter “unlensed- $\Lambda$ CDM”), ii) simulations generated from those same input skies, explicitly lensed in map space as described below (hereafter “lensed- $\Lambda$ CDM”), and iii) simulations containing only tensor  $B$ -modes with  $r = 0.2$  (and  $n_t = 0$ ).

##### 5.1.1. Constrained input maps

The observing matrix and purification operator described in §6.2 are constructed for a specific assumed  $T$  sky map. Since its construction is computationally very expensive it is preferable to constrain the input  $T$  skies used for the simulations to be the same rather than to recalculate the operator for each simulation.

To construct constrained  $Q$  and  $U$  sky maps which respect the known  $\Lambda$ CDM  $TE$  correlation we start from a map of the well measured temperature anisotropy, specifically the *Planck* Needlet Internal Linear Combination (NILC)  $T$  map<sup>21</sup>. We calculate the  $a_{\ell m}^T$  using the *synfast* software from the *Healpix*<sup>22</sup> package (Górski et al. 2005), and then calculate sets of  $a_{\ell m}^E$  using

$$a_{\ell m}^E = \frac{C_\ell^{TE}}{C_\ell^{TT}} a_{\ell m}^T + \sqrt{C_\ell^{EE} - (C_\ell^{TE})^2 / C_\ell^{TT}} n_{\ell m} \quad (1)$$

<sup>21</sup> [http://irsa.ipac.caltech.edu/data/Planck/release\\_1/all-sky-maps/previews/COM\\_CompMap\\_CMB-nilc\\_2048\\_R1\\_20/index.html](http://irsa.ipac.caltech.edu/data/Planck/release_1/all-sky-maps/previews/COM_CompMap_CMB-nilc_2048_R1_20/index.html)

<sup>22</sup> <http://healpix.sourceforge.net/>

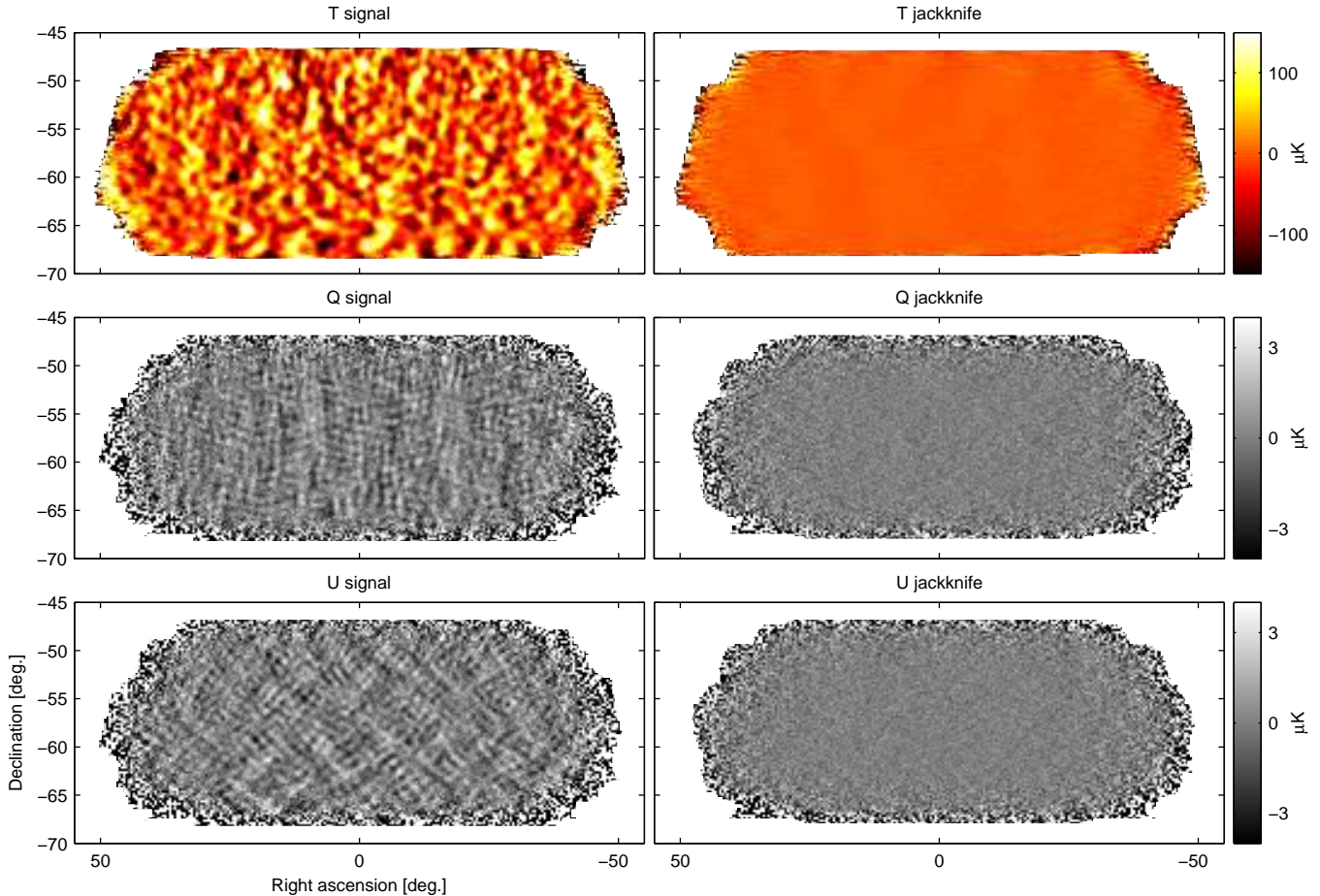


FIG. 1.— BICEP2  $T$ ,  $Q$ ,  $U$  maps. The left column shows the basic signal maps with  $0.25^\circ$  pixelization as output by the reduction pipeline. The right column shows difference (jackknife) maps made with the first and second halves of the data set. No additional filtering other than that imposed by the instrument beam (FWHM  $0.5^\circ$ ) has been done. Note that the structure seen in the  $Q$  &  $U$  signal maps is as expected for an  $E$ -mode dominated sky.

where the  $C_\ell$ 's are  $\Lambda$ CDM spectra from CAMB<sup>23</sup> with cosmological parameters taken from Planck Collaboration XVI (2013), and the  $n_{\ell m}$  are normally distributed complex random numbers. For  $C_\ell^{TT}$  we use a lensed- $\Lambda$ CDM spectrum since the  $a_{\ell m}^T$  from *Planck* NILC inherently contain lensing. We have found the noise level in the *Planck* NILC maps for our region of observation and multipole range to be low enough that it can be ignored.

Using the  $a_{\ell m}^E$  we generate  $N_{\text{side}}=2048$  maps using *synfast*. We substitute in the  $a_{\ell m}^T$  from *Planck* 143 GHz so that the  $T$  map more closely resembles the  $T$  sky we expect to see with BICEP2. (This is also the map that is used in §4.6 to construct deprojection templates.) Additionally, we add in noise to the  $T$  map at the level predicted by the noise covariance in the *Planck* 143 GHz map, which allows us to simulate any deprojection residual due to noise in the *Planck* 143 GHz map.

### 5.1.2. Lensing of input maps

Lensing is added to the unlensed- $\Lambda$ CDM maps using the *LensPix*<sup>24</sup> software (Lewis 2011). We use this software to generate lensed versions of the constrained CMB input  $a_{\ell m}$ 's described in §5.1.1. Input to the lensing operation are deflection angle spectra that are generated with CAMB as part of the

standard computation of  $\Lambda$ CDM spectra. The lensing operation is performed before the beam smoothing is applied to form the final map products. We do not apply lensing to the 143 GHz temperature  $a_{\ell m}^T$  from *Planck* since these inherently contain lensing. Our simulations hence approximate lensed CMB maps ignoring the lensing correlation between  $T$  and  $E$ .

### 5.2. Noise Pseudo Simulations

The previous BICEP1 and QUAD pipelines used a Fourier based procedure to make simulated noise timestreams, maintaining correlations between all channels (Pryke et al. 2009). For the increased channel count in BICEP2 this is computationally very expensive, so we have switched to an alternate procedure adapted from van Engelen et al. (2012). We perform additional coadds of the real pairmaps randomly flipping the sign of each scanset. The sign-flip sequences are constructed such that the total weight of positively and negatively weighted maps is equal. We have checked this technique against the older technique, and against another technique which constructs map noise covariance matrices, and have found them all to be equivalent to the relevant level of accuracy. By default we use the sign flipping technique and refer to these realizations as “noise pseudo simulations.”

We add the noise maps to the lensed- $\Lambda$ CDM realizations to form signal plus noise simulations — hereafter referred to as lensed- $\Lambda$ CDM+noise.

<sup>23</sup><http://camb.info/>

<sup>24</sup><http://cosmologist.info/lenspix/>

## 6. FROM MAPS TO POWER SPECTRA

6.1. *Inversion to Spectra*

The most basic power spectrum estimation procedure which one can employ is to apply an apodization windowing, Fourier transform, construct  $E$  and  $B$  from  $Q$  and  $U$ , square, and take the means in annuli as estimates of the CMB bandpowers. A good choice for the window may be the inverse of the noise variance map (or a smoothed version thereof). Employing this simple procedure on the unlensed- $\Lambda$ CDM simulations we find an unacceptable degree of  $E$  to  $B$  mixing. While such mixing can be corrected for in the mean using simulations, its fluctuation leads to a significant loss of sensitivity.

There are several things which can cause  $E$  to  $B$  mixing: i) the “sky-cut” implied by the apodization window (the transformation from  $Q$  and  $U$  to  $E$  and  $B$  is non-local so some of the modes around the edge of the map are ambiguous), ii) the timestream (and therefore map) filtering which we have imposed in §4.1 and §4.6, and iii) the simple RA/Dec. map projection which we have chosen.

To correct for sky-cut induced mixing improved estimators have been suggested. We first tried implementing the estimator suggested by Smith (2006) which takes Fourier transforms of products of the map with various derivatives of the apodization window. However, testing on the unlensed- $\Lambda$ CDM simulations revealed only a modest improvement in performance since this estimator does not correct mixing caused by filtering of the map.

6.2. *Matrix Based Map Purification*

To overcome the  $E$  to  $B$  mixing described in the previous subsection we have introduced an additional purification step after the  $Q$  and  $U$  maps are formed. This step has to be performed in pixel space where the filtering takes place. In parallel with the construction of the pairmaps and their accumulation we construct pixel-pixel matrices which track how every true sky pixel maps into the pixels of our final coadded map due to the various filtering operations. We take “true sky pixel maps” to be  $N_{\text{side}}=512$  Healpix maps, whose pixel size ( $\sim 0.1^\circ$  on a side) is smaller than our observed map pixels ( $0.25^\circ$ ). The act of simulating our various filtering operations becomes a simple matrix multiplication:

$$\tilde{\mathbf{m}} = \mathbf{R}\mathbf{m} \quad (2)$$

where  $\mathbf{m}$  is a vector consisting of  $[Q, U]$  values for each Healpix pixel and  $\tilde{\mathbf{m}}$  is a  $[Q, U]$  vector as observed by BICEP2 in the absence of noise.

Next, we “observe” an  $N_{\text{side}}=512$  Healpix theoretical covariance matrix<sup>25</sup>,  $\mathbf{C}$ , with  $\mathbf{R}$ :

$$\tilde{\mathbf{C}} = \mathbf{R}\mathbf{C}\mathbf{R}^T \quad (3)$$

We form  $\tilde{\mathbf{C}}$  for both  $E$ -mode and  $B$ -mode covariances. These matrices provide the pixel-pixel covariance for  $E$ -modes and  $B$ -modes in the same observed space as the real data. However, the matrix  $\mathbf{R}$  has made the two spaces non-orthogonal and introduced ambiguous modes, i.e. modes in the observed space which are superpositions of either  $E$ -modes or  $B$ -modes on the sky.

To isolate the pure  $B$ -modes we adapt the method described in Bunn et al. (2003). We solve a generalized eigenvalue

problem:

$$(\tilde{\mathbf{C}}_B + \sigma^2 \mathbf{I})\mathbf{b} = \lambda_b (\tilde{\mathbf{C}}_E + \sigma^2 \mathbf{I})\mathbf{b} \quad (4)$$

where  $\mathbf{b}$  is a  $[Q, U]$  eigenmode and  $\sigma^2$  is a small number introduced to regularize the problem. By selecting modes corresponding to the largest eigenvalues  $\lambda_b \gg 1$ , we can find the  $B$ -mode subspace of the observed sky which is orthogonal to  $E$ -modes and ambiguous modes. The covariance matrices are calculated using steeply reddened input spectra ( $\sim 1/\ell^2$ ) so that the eigenmodes are separated in angular scale, making it easy to select modes up to a cutoff  $\ell$  set by the instrument resolution.

The matrix purification operator is a sum of outer products of the selected eigenmodes; it projects an input map onto this space of pure  $B$ -modes:

$$\Pi_b = \sum_i \mathbf{b}_i \mathbf{b}_i^T \quad (5)$$

It can be applied to any simulated map vector ( $\tilde{\mathbf{m}}$ ) and returns a purified vector which contains only signal coming from  $B$ -modes on the true sky:

$$\tilde{\mathbf{m}}_{\text{pure}} = \Pi_b \tilde{\mathbf{m}} \quad (6)$$

This method is superior to the other methods discussed above because it removes the  $E$ -to- $B$  leakage resulting from the filterings and the sky-cut, because  $\mathbf{R}$  contains all of these steps. After the purification, in the present analysis we use the simple power spectrum estimation described in the previous subsection, although in the future we may switch to a fully matrix-based approach.

Testing this operator on the standard unlensed- $\Lambda$ CDM simulations (which are constructed entirely independently) we empirically determine that it is extremely effective, with residual false  $B$ -modes corresponding to  $r < 10^{-4}$ . Testing the operator on the  $r = 0.2$  simulations we find that it produces only a very modest increase in the sample variance — i.e. the fraction of mixed (ambiguous) modes is found to be small.

6.3. *Noise Subtraction and Filter/Beam Correction*

As is standard procedure in the MASTER technique (Hivon et al. 2002), we noise debias the spectra by subtracting the mean of the noise realizations (see §5.2). The noise in our maps is so low that this is a relevant correction only for  $BB$ , although we do it for all spectra.

To determine the response of each observed bandpower to each multipole on the sky we run special simulations with delta function spectra input to `synfast` multiplied by the average measured beam function. Taking the mean over many realizations<sup>26</sup> we determine the “bandpower window functions” (BPWF) (Knox 1999). The integral of these functions is the factor by which each bandpower has been suppressed by the instrument beam and all filterings (including the matrix purification). We therefore divide by these factors and re-normalize the BPWF to unit sum. This is a variant on the standard MASTER technique. (We choose to plot the bandpower values at the weighted mean of the corresponding BPWF instead of at the nominal band center, although this has a significant effect only on the lowest one.)

<sup>25</sup> Constructed following Appendix A of Tegmark & de Oliveira-Costa (2001).

<sup>26</sup> To enable the 600 multipoles  $\times$  100 realizations per multipole required we do “short-cut” simulations using the observing matrix  $\mathbf{R}$  mentioned in §6.2 above rather than the usual explicit timestream simulations. These are empirically found to be equivalent to high accuracy.

One point worth emphasizing is that when comparing the real data to our simulations (or jackknife differences thereof) the noise subtraction and filter/beam corrections have no effect since they are applied equally to the real data and simulations. The BPWFs are required to compare the final bandpowers to an arbitrary external theoretical model and are provided with the data release.

The same average measured beam function is used in the signal simulations and in the BPWF calculation. In as much as this function does not reflect reality the real bandpowers will be under or over corrected at high  $\ell$ . We estimate the beam function uncertainty to be equivalent to a 1.1% width error on a 31 arcminute FWHM Gaussian.

## 7. RESULTS

### 7.1. Power Spectra

Following the convention of C10 and B14 we report nine bandpowers, each  $\approx 35$  multipoles wide and spanning the range  $20 < \ell < 340$ . Figure 2 shows the BICEP2 power spectra<sup>27</sup>. With the exception of *BB* all spectra are consistent with their lensed- $\Lambda$ CDM expectation values — the probability to exceed (PTE) the observed value of a simple  $\chi^2$  statistic is given on the plot (as evaluated against simulations — see §7.3).

*BB* appears consistent with the lensing expectation at higher  $\ell$ , but at lower multipoles there is an excess which is detected with high signal-to-noise. The  $\chi^2$  of the data is much too high to allow us to directly evaluate the PTE of the observed value under lensed- $\Lambda$ CDM using the simulations. We therefore “amplify” the Monte Carlo statistics by resampling bandpower values from distributions fit to the simulated ones. For the full set of nine bandpowers shown in the figure we obtain a PTE of  $1.3 \times 10^{-7}$  equivalent to a significance of  $5.3\sigma$ . Restricting to the first five bandpowers ( $\ell \lesssim 200$ ) this changes to  $5.2\sigma$ . We caution against over interpretation of the two high bandpowers at  $\ell \approx 220$  — their joint significance is  $< 3\sigma$  (also see Figure 9).

Figure 2 also shows the temporal-split jackknife — the spectrum produced when differencing maps made from the first and second halves of the data. The *BB* excess is not seen in the jackknife, which rules out misestimation of the noise debias as the cause (the noise debias being equally large in jackknife spectra).

### 7.2. E and B Maps

Once we have the sets of *E* and *B* Fourier modes, instead of collapsing within annuli to form power spectra, we can instead reinvert to make apodized *E* and *B* maps. In Figure 3 we show such maps prepared using exactly the same Fourier modes as were used to construct the spectra shown in Figure 2 filtering to the range  $50 < \ell < 120$ . In comparison to the simulated maps we see i) BICEP2 has detected *B*-modes with high signal-to-noise ratio *in the map*, and ii) this signal appears to be evenly distributed over the field, as is the expectation for a cosmological signal, but generally will not be for a Galactic foreground.

### 7.3. Internal Consistency Tests

We evaluate the consistency of the jackknife spectra with their  $\Lambda$ CDM expectations by using a simple  $\chi^2$  statistic,

<sup>27</sup> These bandpowers along with all the ancillary data required to use them are available for download at [http://bicepkeck.org/bicep2\\_2014\\_release](http://bicepkeck.org/bicep2_2014_release).

$$\chi^2 = (\mathbf{d} - \langle \mathbf{m} \rangle)^T \mathbf{D}^{-1} (\mathbf{d} - \langle \mathbf{m} \rangle) \quad (7)$$

where  $\mathbf{d}$  is the vector of observed bandpower values,  $\langle \mathbf{m} \rangle$  is the mean of the lensed- $\Lambda$ CDM+noise simulations, and  $\mathbf{D}$  is the bandpower covariance matrix as evaluated from those simulations<sup>28</sup>. We also compute  $\chi^2$  for each of the simulations<sup>29</sup> and take the probability to exceed (PTE) the observed value versus the simulated distribution. In addition to  $\chi^2$  we compute the sum of normalized deviations,

$$\chi = \sum_i \frac{d_i - \langle m_i \rangle}{\sigma_{m_i}} \quad (8)$$

where the  $d_i$  are the observed bandpower values and  $\langle m_i \rangle$  and  $\sigma_{m_i}$  are the mean and standard deviation of the lensed- $\Lambda$ CDM+noise simulations. This statistic tests for sets of bandpowers which are consistently all above or below the expectation. Again we evaluate the PTE of the observed value against the distribution of the simulations.

We evaluate these statistics both for the full set of nine bandpowers (as in C10 and B14), and also for the lower five of these corresponding to the multipole range of greatest interest ( $20 < \ell < 200$ ). Numerical values are given in Table 1 and the distributions are plotted in Figure 4. Since we have 500 simulations the minimum observable non zero value is 0.002. Most of the *TT*, *TE* and *TB* jackknives pass, but following C10 and B14 we omit them from formal consideration (and they are not included in the table and figure). The signal-to-noise in *TT* is  $\sim 10^4$  so tiny differences in absolute calibration between the data subsets can cause jackknife failure, and the same is true to a lesser extent for *TE* and *TB*. Even in *EE* the signal-to-noise is approaching  $\sim 10^3$  (500 in the  $\ell \approx 110$  bin) and careful examination of the table shows marginal values for the tile jackknife in this spectrum. However with a maximum signal-to-noise ratio of  $\lesssim 10$  in *BB* such calibration differences are not a concern and all the *BB* (and *EB*) jackknives are seen to pass.

To form the jackknife spectra we difference the maps made from the two halves of the data split, divide by two, and take the power spectrum. This holds the power spectrum amplitude of a contribution which is uncorrelated in the two halves (such as noise) constant, while a fully correlated component (such as sky signal) cancels perfectly. The amplitude of a component which appears only in one half will stay the same under this operation as it is in the fully coadded map *and the apparent signal-to-noise will also stay the same*. For a noise-dominated experiment this means that jackknife tests can only limit potential contamination to a level comparable to the noise uncertainty. However the *BB* bandpowers shown in Figure 2 have signal-to-noise as high as 10. This means that jackknife tests are extremely powerful in our case — the reductions in power which occur in the jackknife spectra are empirical proof that the *B*-mode pattern on the sky is highly correlated between all data splits considered.

<sup>28</sup> Due to differences in sky coverage between the two halves of a jackknife split, in conjunction with filtering, the expectation value of some of the jackknives is not quite zero — hence we always evaluate  $\chi^2$  versus the mean of the simulations. Because the BPWF overlap slightly adjacent bandpowers are  $\lesssim 10\%$  correlated. We zero all but the main and first off-diagonal elements of  $\mathbf{D}$  as the other elements are not measured above noise given the limited simulation statistics.

<sup>29</sup> Recomputing  $\mathbf{D}$  each time, excluding that simulation.

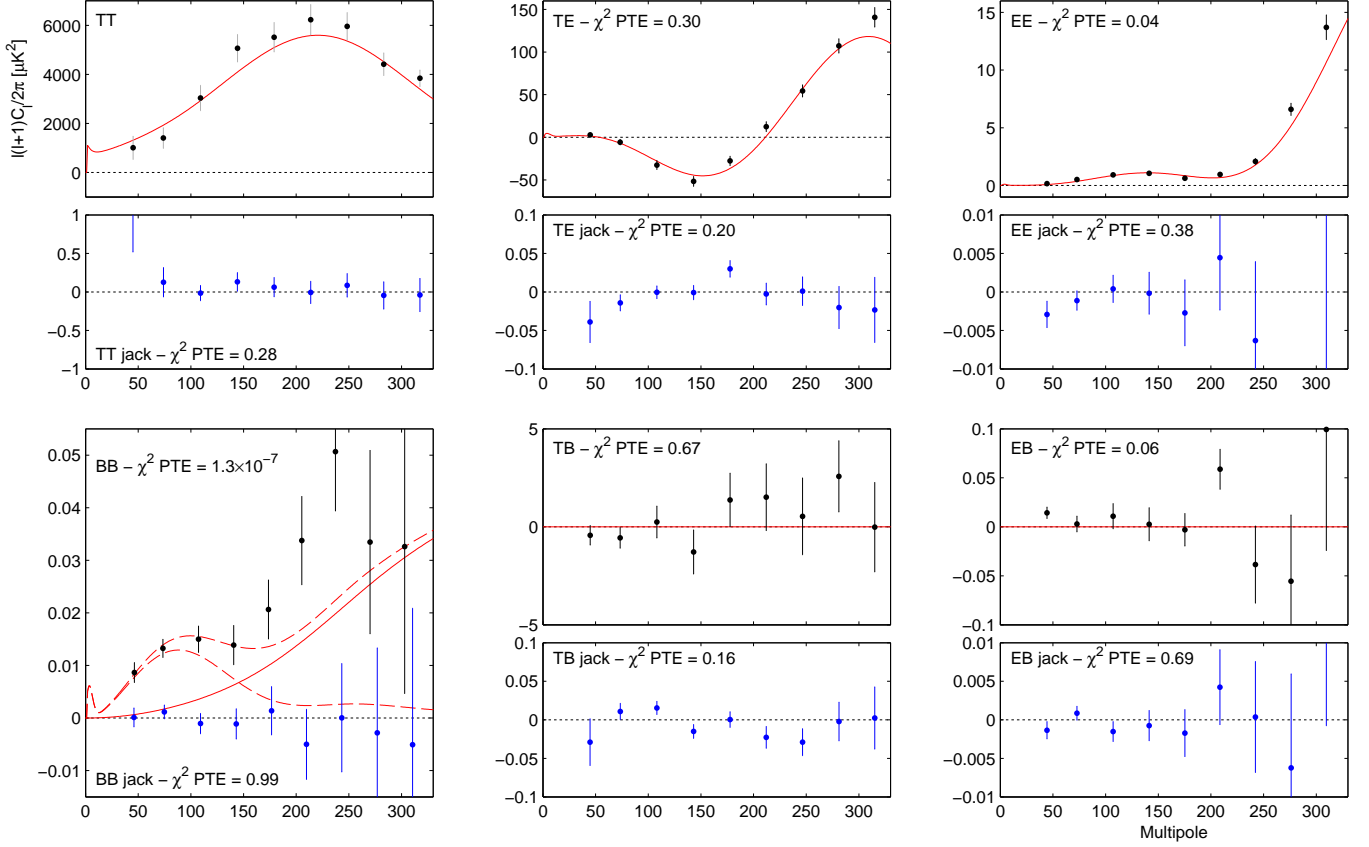


FIG. 2.— BICEP2 power spectrum results for signal (black points) and temporal-split jackknife (blue points). The red curves show the lensed- $\Lambda$ CDM theory expectations — in the case of  $BB$  an  $r = 0.2$  spectrum is also shown. The error bars are the standard deviations of the lensed- $\Lambda$ CDM+noise simulations. The probability to exceed (PTE) the observed value of a simple  $\chi^2$  statistic is given (as evaluated against the simulations). Note the very different y-axis scales for the jackknife spectra (other than  $BB$ ). See the text for additional discussion of the  $BB$  spectrum.

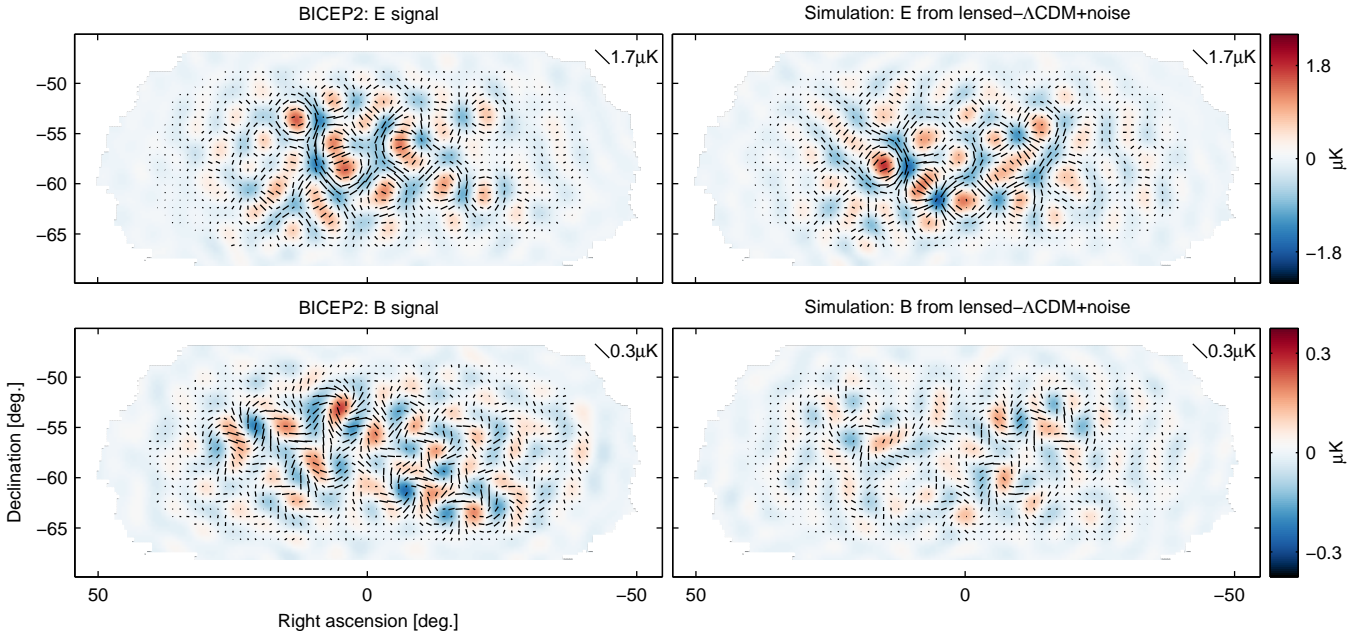


FIG. 3.— *Left*: BICEP2 apodized  $E$ -mode and  $B$ -mode maps filtered to  $50 < \ell < 120$ . *Right*: The equivalent maps for the first of the lensed- $\Lambda$ CDM+noise simulations. The color scale displays the  $E$ -mode scalar and  $B$ -mode pseudoscalar patterns while the lines display the equivalent magnitude and orientation of linear polarization. Note that excess  $B$ -mode is detected over lensing+noise with high signal-to-noise in the map ( $s/n > 2$  per map mode at  $\ell \approx 70$ ). (Also note that the  $E$ -mode and  $B$ -mode maps use different color/length scales.)

TABLE 1  
JACKKNIFE PTE VALUES FROM  $\chi^2$  AND  $\chi$  (SUM-OF-DEVIATION)  
TESTS

Jackknife	Bandpowers 1–5 $\chi^2$	Bandpowers 1–9 $\chi^2$	Bandpowers 1–5 $\chi$	Bandpowers 1–9 $\chi$
<b>Deck jackknife</b>				
EE	0.046	0.030	0.164	0.299
BB	0.774	0.329	0.240	0.082
EB	0.337	0.643	0.204	0.267
<b>Scan Dir jackknife</b>				
EE	0.483	0.762	0.978	0.938
BB	0.531	0.573	0.896	0.551
EB	0.898	0.806	0.725	0.890
<b>Temporal Split jackknife</b>				
EE	0.541	0.377	0.916	0.938
BB	0.902	0.992	0.449	0.585
EB	0.477	0.689	0.856	0.615
<b>Tile jackknife</b>				
EE	0.004	0.010	0.000	0.002
BB	0.794	0.752	0.565	0.331
EB	0.172	0.419	0.962	0.790
<b>Azimuth jackknife</b>				
EE	0.673	0.409	0.126	0.339
BB	0.591	0.739	0.842	0.944
EB	0.529	0.577	0.840	0.659
<b>Mux Col jackknife</b>				
EE	0.812	0.587	0.196	0.204
BB	0.826	0.972	0.293	0.283
EB	0.866	0.968	0.876	0.697
<b>Alt Deck jackknife</b>				
EE	0.004	0.004	0.070	0.236
BB	0.397	0.176	0.381	0.086
EB	0.150	0.060	0.170	0.291
<b>Mux Row jackknife</b>				
EE	0.052	0.178	0.653	0.739
BB	0.345	0.361	0.032	0.008
EB	0.529	0.226	0.024	0.048
<b>Tile/Deck jackknife</b>				
EE	0.048	0.088	0.144	0.132
BB	0.908	0.840	0.629	0.269
EB	0.050	0.154	0.591	0.591
<b>Focal Plane inner/outer jackknife</b>				
EE	0.230	0.597	0.022	0.090
BB	0.216	0.531	0.046	0.092
EB	0.036	0.042	0.850	0.838
<b>Tile top/bottom jackknife</b>				
EE	0.289	0.347	0.459	0.599
BB	0.293	0.236	0.154	0.028
EB	0.545	0.683	0.902	0.932
<b>Tile inner/outer jackknife</b>				
EE	0.727	0.533	0.128	0.485
BB	0.255	0.086	0.421	0.036
EB	0.465	0.737	0.208	0.168
<b>Moon jackknife</b>				
EE	0.499	0.689	0.481	0.679
BB	0.144	0.287	0.898	0.858
EB	0.289	0.359	0.531	0.307
<b>A/B offset best/worst</b>				
EE	0.317	0.311	0.868	0.709
BB	0.114	0.064	0.307	0.094
EB	0.589	0.872	0.599	0.790

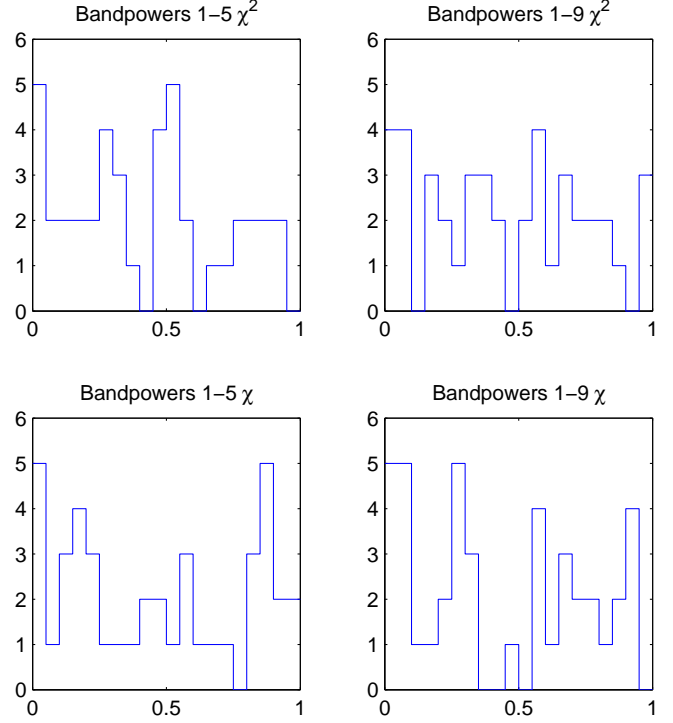


FIG. 4.— Distributions of the jackknife  $\chi^2$  and  $\chi$  PTE values over the 14 tests and three spectra given in Table 1. These distributions are consistent with uniform.

We have therefore conducted an unusually large number of jackknife tests trying to imagine data splits which might conceivably contain differing contamination. Here we briefly describe each of these:

BICEP2 observed at deck angles of  $68^\circ$ ,  $113^\circ$ ,  $248^\circ$  and  $293^\circ$ . We can split these in two ways without losing the ability to make  $Q$  and  $U$  maps (see §4.7). The *deck jack* is defined as  $68^\circ$  and  $113^\circ$  vs.  $248^\circ$  and  $293^\circ$  while the *alt. deck jack* is  $68^\circ$  and  $293^\circ$  vs.  $113^\circ$  and  $248^\circ$ . Uniform differential pointing averages down in a coaddition of data including an equal mix of  $180^\circ$  complement angles, but it will be amplified in either of these jackknives (as we see in our simulations). The fact that we are passing these jackknives indicates that residual beam systematics of this type are subdominant after deprojection.

The *temporal-split* simply divides the data into two equal weight parts sequentially. Similarly, but at the opposite end of the time scale range, we have the *scan direction* jackknife, which differences maps made from the right and left going half-scans, and is sensitive to errors in the detector transfer function.

The *azimuth* jackknife differences data taken over different ranges of telescope azimuth angle — i.e. with different potential contamination from fixed structures or emitters on the ground. A related category is the *moon* jackknife, which differences data taken when the moon is above and below the horizon.

A series of jackknives tests if the signal originates in some subset of the detector pairs. The *tile* jackknife tests tiles 1 and 3 vs. 2 and 4 (this combination being necessary to get reasonable coverage in the  $Q$  and  $U$  maps). Similarly the *tile inner/outer* and *tile top/bottom* jackknives are straightforward. The *focal plane inner/outer* does as stated for the entire focal plane and is a potentially powerful test for imperfections

which increase radially. The *mux row* and *mux column* jackknives test for systematics originating in the readout system.

The *tile/deck* jackknife tests for a possible effect coming from always observing a given area of sky with detectors the “same way up”, although due to the small range of the elevation steps it is limited to a small sky area.

Finally we have performed one test based on beam non-ideality as observed in external beam map runs. The *A/B offset best/worst* jackknife differences the best and worst halves of the detector pairs as selected by that metric.

See the Systematics Paper for a full description of the jackknife studies.

## 8. SYSTEMATIC UNCERTAINTIES

Within the simulation-calibrated analysis framework described above we are free to perform any arbitrary filtering of the data which may be necessary to render the results insensitive to particular systematics. However, as such mode removal increases the uncertainty of the final bandpowers, we clearly wish to filter only systematics which might induce false *B*-mode at relevant levels. Moreover it may not be computationally feasible to construct simple timestream templates for some potential systematics. Therefore once we have made our selection as to which filterings to perform we must then estimate the residual contamination and either subtract it or show it to be negligible.

To guide our selection of mode removal we have two main considerations. First, we can examine jackknives of the type described in §7.3 above — reduction in failures with increasing mode removal may imply that a real systematic effect is present. Second, and as we will see below more powerfully, we can examine external calibration data (principally beam maps) to directly calculate the false *B*-mode expected from specific effects.

### 8.1. Simulations Using Observed Per Channel Beam Shapes

As described in the Instrument Paper we have made extremely high signal-to-noise in situ measurements of the far-field beam shape of each channel. Fitting these beams to elliptical Gaussians we obtain differential parameters that correlate well with the mean value of the deprojection coefficients from §4.6. One may then ask whether it would be better to subtract rather than deproject. In general it is more conservative to deproject as this i) allows for the possibility that the coefficients are changing with time, and ii) is guaranteed to completely eliminate the effect in the mean, rather than leaving a residual bias due to noise on the subtraction coefficients.

We use the per-channel beam maps as inputs to special *T*-only input simulations and measure the level of *T* to *B* mixing while varying the set of beam-modes being deprojected. The beam maps do not provide a good estimate of differential gain so we substitute estimates which come from a per-channel variant of the absolute calibration procedure mentioned in §4.7 above. The left panel of Figure 5 shows *B*-mode power spectra from these simulations under the following deprojections i) none, ii) differential pointing only, iii) differential pointing and differential gain, iv) differential pointing, differential gain and differential beam width, and v) differential pointing, differential gain and differential ellipticity.

We see that differential pointing has the largest effect and so to be conservative we choose to deproject it. Differential gain is also seen to be a significant effect and we again deproject it — we lack independent subtraction coefficients, and it might plausibly be time variable. Differential beam width

is a negligible effect and we do not deproject it. Differential ellipticity is also a small effect. We find in the simulations that deprojection of differential ellipticity interacts with real *TE* correlation in a complex manner slightly distorting the *TE* spectrum. We therefore choose to subtract this effect by fixing the coefficients to their beam map derived values in §4.6. Whether differential ellipticity is deprojected or subtracted makes no significant difference to any of the spectra other than *TE*. Finally we make a small correction for the undeprojected residual by subtracting the final curve in the left panel of Figure 5 from the results presented in §7. (The correction is equivalent to  $r = 0.001$ .) We also increase the bandpower fluctuation to reflect the post-correction upper limit on extended beam mismatch shown in the right panel of Figure 5. See the Systematics Paper for details.

### 8.2. Overall Polarization Rotation

Once differential ellipticity has been corrected we notice that an excess of *TB* and *EB* power remains at  $\ell > 200$  versus the  $\Lambda$ CDM expectation. The spectral form of this power is consistent with an overall rotation of the polarization angle of the experiment. While the detector-to-detector relative angles have been measured to differ from the design values by  $< 0.2^\circ$  we currently do not have an accurate external measurement of the overall polarization angle. We therefore apply a rotation of  $\sim 1^\circ$  to the final *Q/U* maps to minimize the *TB* and *EB* power (Keating et al. 2013; Kaufman et al. 2013). We emphasize that this has a negligible effect on the *BB* bandpowers at  $\ell < 200$ .

### 8.3. Other Possible Systematics

Many other systematics can be proposed as possibly leading to false *B*-modes at a relevant level. Some possible effects will produce jackknife failure before contributing to the non-jackknife *B*-mode power at a relevant level. Limits on others must be set by external data or other considerations. Any azimuth fixed effect, such as magnetic pickup, is removed by the scan-synchronous template removal mentioned in §3.1 and §4.

We have attempted an exhaustive consideration of all possible effects — a brief summary will be given here with the details deferred to the Systematics Paper. The right panel of Figure 5 shows estimated levels of, or upper limits on, contamination from extended beam mismatch after the undeprojected residual correction, thermal drift in the focal plane, systematic polarization angle miscalibration, randomized polarization angle miscalibration, ghost beams, detector transfer function mismatch, and crosstalk. The upper limit for extended beam mismatch is the  $1\sigma$  uncertainty on contamination predicted from beam map simulations identical to those described in §8.1 but using a larger region of the beam. (Note that this will include beam or beam-like effects which are present in the beam mapping runs, including crosstalk and sidelobes at  $\lesssim 4^\circ$ .) For systematic polarization angle miscalibration it is the level at which such an error would produce a detectable *TB* signal with 95% confidence. For randomized polarization angle miscalibration, it is the leakage we would incur from assuming nominal polarization angles, i.e. no ability to measure per-pair relative polarization angles. For thermal drift, it is the noise floor set by the sensitivity of the thermistors that monitor focal plane temperature.

## 9. FOREGROUND PROJECTIONS

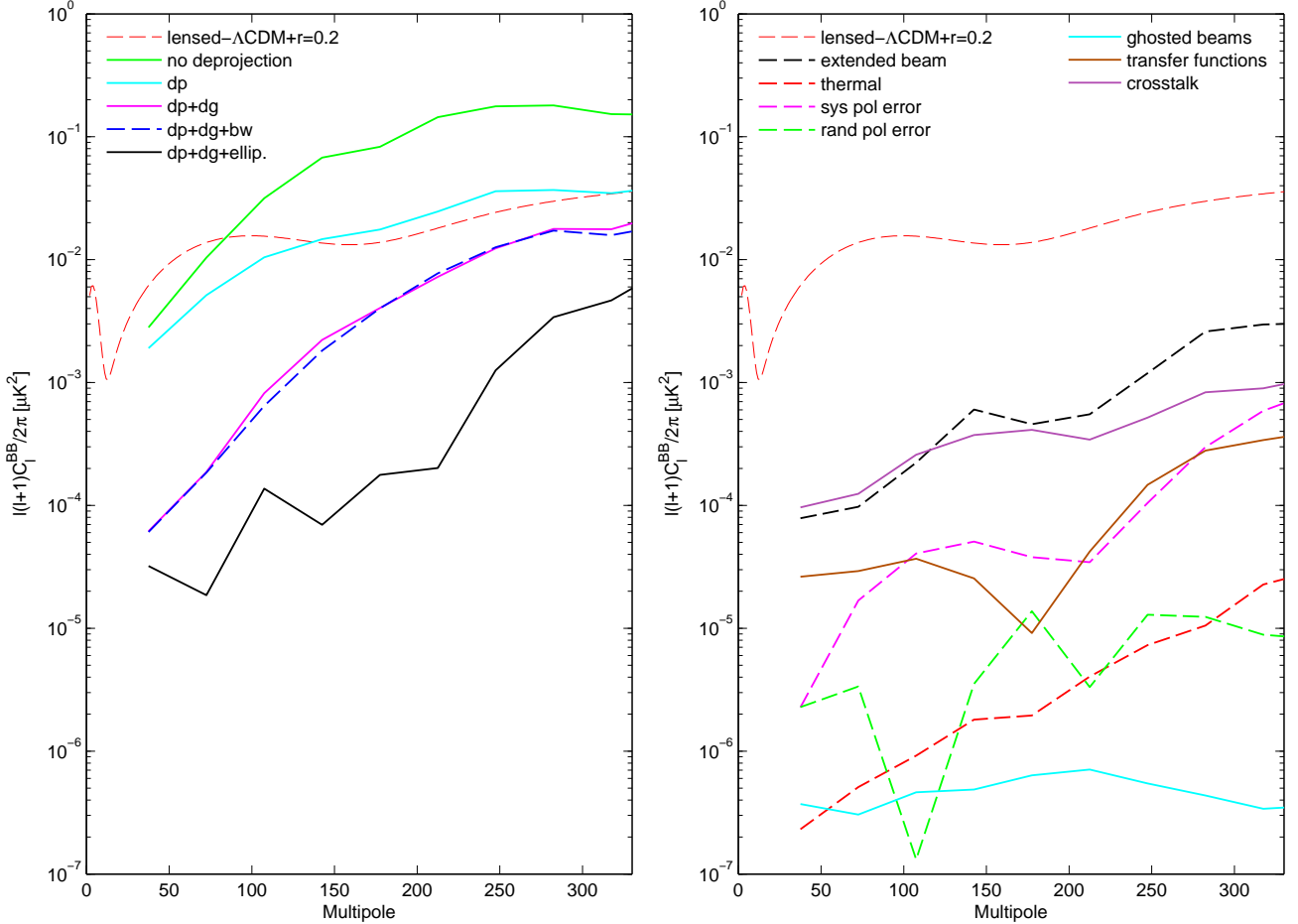


FIG. 5.— *Left:*  $BB$  spectra from  $T$ -only input simulations using the measured per channel beam shapes compared to the lensed- $\Lambda$ CDM+r=0.2 spectrum. From top to bottom the curves are i) no deprojection, ii) deprojection of differential pointing and differential gain of the detector pairs (dp+dg), iii) deprojection of differential pointing and differential gain of the detector pairs (dp+dg), iv) adding deprojection of differential beam width (dp+dg+bw), and v) differential pointing, differential gain and differential ellipticity (dp+dg+ellip.). *Right:* Estimated levels of other systematics as compared to the lensed- $\Lambda$ CDM+r=0.2 spectrum. Solid lines indicate expected contamination. Dashed lines indicate upper limits. All systematics are comparable to or smaller than the extended beam mismatch upper limit.

Having established that the detected  $B$ -mode signal is not an instrumental artifact, we now consider whether it might be due to a Galactic or extragalactic foreground. At low or high frequencies Galactic synchrotron and polarized-dust emission, respectively, are the dominant foregrounds. The intensity of both falls rapidly with increasing Galactic latitude but dust emission falls faster. The equal amplitude cross-over frequency therefore rises to  $\gtrsim 100$  GHz in the cleanest regions (Dunkley et al. 2009, Fig. 10). The BICEP2 field is centered on Galactic coordinates  $(l, b) = (316^\circ, -59^\circ)$  and was originally selected on the basis of exceptionally low contrast in the FDS dust maps (Finkbeiner et al. 1999). It must be emphasized that these ultra clean regions are very special — at least an order of magnitude cleaner than the average  $b > 50^\circ$  level.

Foreground modeling involves extrapolating high signal-to-noise ratio maps taken at lower/higher frequencies to the CMB observation band, and there are inevitably uncertainties. Many previous studies have been conducted and projections made — see for instance Dunkley et al. (2009) and references therein. We note that such studies generically predict levels of foreground  $B$ -mode contamination in clean high latitude regions equivalent to  $r \lesssim 0.01$  — well below that which we observe.

### 9.1. Polarized Dust Projections

The main uncertainty in foreground modeling is currently the lack of a polarized dust map. (This will be alleviated soon by the next *Planck* data release.) In the meantime we have therefore investigated a number of existing models and have formulated two new ones. A brief description of each model is as follows:

**FDS:** Model 8 (Finkbeiner et al. 1999), assuming a uniform polarization fraction of 5% and setting  $Q = U$ .

**BSS:** Bi-Symmetric Spiral (BSS) model of the Galactic magnetic field (O’Dea et al. 2012)<sup>30</sup>.

**LSA:** Logarithmic Spiral Arm (LSA) model of the Galactic magnetic field (O’Dea et al. 2012)<sup>30</sup>.

**PSM:** Planck Sky Model (PSM) (Delabrouille et al. 2013) version 1.7.8, run as a “Prediction” with 15% dust intrinsic polarization fraction and Galactic magnetic field pitch angle of  $-30^\circ$ <sup>31</sup>.

**DDM1:** “Data Driven Model 1” (DDM1) constructed from publicly available *Planck* data products. The *Planck* dust model map at 353 GHz is scaled to 150 GHz assuming a con-

<sup>30</sup><http://www3.imperial.ac.uk/people/c.contaldi/fgpol>

<sup>31</sup><http://www.apc.univ-paris7.fr/~delabrou/PSM/psm.html>

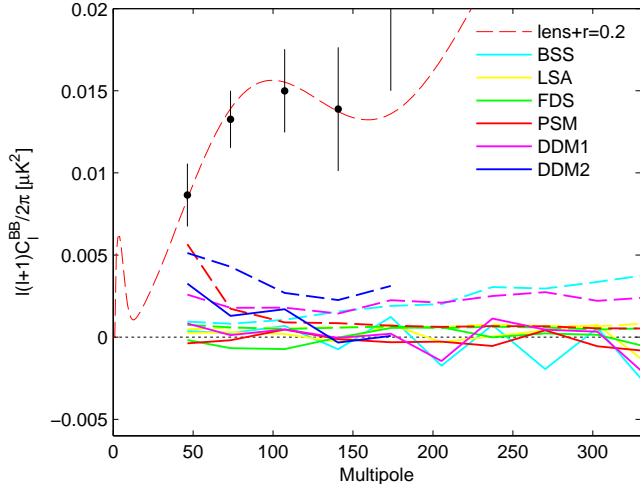


FIG. 6.— Polarized dust foreground projections for our field using various models available in the literature, and two new ones formulated using publicly available information from *Planck*. Dashed lines show auto-spectra of the models, while solid lines show cross spectra between the models and the BICEP2 maps. The cross spectra are consistent with zero, and the DDM2 auto spectrum (at least) is noise biased high (and is hence truncated to  $\ell < 200$ ). The BICEP2 auto spectrum from Figure 2 is also shown with the lensed- $\Lambda$ CDM+ $r = 0.2$  spectrum.

stant emissivity value of 1.6 and a constant temperature of 19.6 K. In our field these values agree both with the mean values shown by the *Planck* Collaboration in dust polarization<sup>32</sup>, and with the median values of the recently delivered *Planck* dust model (Planck Collaboration et al. 2013a). A uniform 5% sky polarization fraction is assumed in agreement with the first all-sky images of dust polarization shown by the *Planck* Collaboration<sup>33</sup>. The polarization angles are taken from the PSM.

**DDM2:** “Data Driven Model 2” (DDM2) constructed using all publicly available information from *Planck*. Uses the same dust model temperature map as DDM1, with polarization fractions and angles matching those shown by the *Planck* Collaboration<sup>33</sup>.

All of the the models except FDS make explicit predictions of the actual polarized dust pattern in our field — presumably with varying probabilities of success. We can therefore search for a correlation between the models and our signal by taking cross spectra against the BICEP2 maps. Figure 6 shows the resulting *BB* auto and cross spectra — note that the auto-spectra are all well below the level of our observed signal and that the cross spectra are consistent with zero<sup>34</sup>. We also note that the DDM2 model auto spectrum (which is the highest) contains uncorrected noise bias from the polarization fraction and angle maps (which is why this curve in Figure 6 is truncated to  $\ell < 200$ ).

### 9.2. Synchrotron

In our field and at angular scales of  $\ell > 30$  the WMAP K-band (23 GHz) maps are noise dominated. Extrapolating them

<sup>32</sup>[http://www.rssd.esa.int/SA/PLANCK/docs/eslab47/Session09\\_Data\\_Processing/47ESLAB\\_April\\_04\\_10\\_30\\_Aumont.pdf](http://www.rssd.esa.int/SA/PLANCK/docs/eslab47/Session09_Data_Processing/47ESLAB_April_04_10_30_Aumont.pdf)

<sup>33</sup>[http://www.rssd.esa.int/SA/PLANCK/docs/eslab47/Session07\\_Galactic\\_Science/47ESLAB\\_April\\_04\\_11\\_25\\_Bernard.pdf](http://www.rssd.esa.int/SA/PLANCK/docs/eslab47/Session07_Galactic_Science/47ESLAB_April_04_11_25_Bernard.pdf)

<sup>34</sup> The cross spectra between each model and real data are consistent with the cross spectra between that model and (uncorrelated) lensed- $\Lambda$ CDM+noise simulations.

to our observing frequency using a spectral index of  $\beta = -3.3$  derived from WMAP foreground products results in an upper limit to synchrotron contamination equivalent to  $r = 0.003$ . Taking the cross spectrum against our observed map indicates that the true value is lower.

### 9.3. Point Sources

Extragalactic point sources might also potentially be a concern. Using the 143 GHz fluxes for the sources in our field from the *Planck* catalog (Planck Collaboration et al. 2013b), together with polarization information from ATCA (Massardi et al. 2011) we find that the contribution to the *BB* spectrum is equivalent to  $r \approx 0.001$ . This is consistent with the projections of Battye et al. (2011).

## 10. CROSS SPECTRA

### 10.1. Cross Spectra with BICEP1

BICEP1 observed essentially the same field as BICEP2 from 2006 to 2008. While a very similar instrument in many ways the focal plane technology of BICEP1 was entirely different, employing horn fed PSBs read out via neutron transmutation-doped (NTD) germanium thermistors (see T10 for details). The high-impedance NTD devices and readouts have different susceptibility to microphonic pickup and magnetic fields, and the shielding of unwanted RFI/EMI was significantly different from that of BICEP2. The beam systematics were also quite different with a more conservative edge taper and a more complex pattern of observed pair centroid offsets. BICEP1 had detectors at both 100 and 150 GHz.

Figure 7 compares the BICEP2 *EE* and *BB* auto spectra with cross spectra taken against the 100 and 150 GHz maps from BICEP1. For *EE* the correlation is extremely strong, which simply confirms that the mechanics of the process are working as expected. For *BB* the signal-to-noise is of course much lower, but there appear to be positive correlations. To test the compatibility of the *BB* auto and cross spectra we take the differences and compare to the differences of lensed- $\Lambda$ CDM+noise+ $r = 0.2$  simulations (which share common input skies)<sup>35</sup>. Using bandpowers 1–5 the  $\chi^2$  and  $\chi$  PTEs are mid-range indicating that the spectra are compatible to within the noise. (This is also true for *EE*.)

Calculating the *BB*  $\chi^2$  and  $\chi$  statistics against the lensed- $\Lambda$ CDM model the BICEP2  $\times$  BICEP1<sub>150</sub> spectrum has PTEs of 0.37 and 0.05 respectively. However, BICEP2  $\times$  BICEP1<sub>100</sub> has PTEs of 0.005 and 0.001 corresponding to  $\approx 3\sigma$  detection of power in the cross spectrum. While it may seem surprising that one cross spectrum shows a stronger detection than the other, it turns out not to be unusual in lensed- $\Lambda$ CDM+noise+ $r = 0.2$  simulations.

### 10.2. Spectral Index Constraint

We can use the BICEP2 auto and BICEP2  $\times$  BICEP1<sub>100</sub> spectra shown in Figure 7 to constrain the frequency dependence of the nominal signal. If the signal at 150 GHz were due to synchrotron we would expect the frequency cross spectrum to be much larger in amplitude than the BICEP2 auto spectrum. Conversely if the 150 GHz power were due to polarized dust emission we would not expect to see a significant correlation with the 100 GHz sky pattern.

<sup>35</sup>For all spectral difference tests we compare against lensed- $\Lambda$ CDM+noise+ $r = 0.2$  simulations as the cross terms between signal and noise increase the variance even for perfectly common sky coverage.

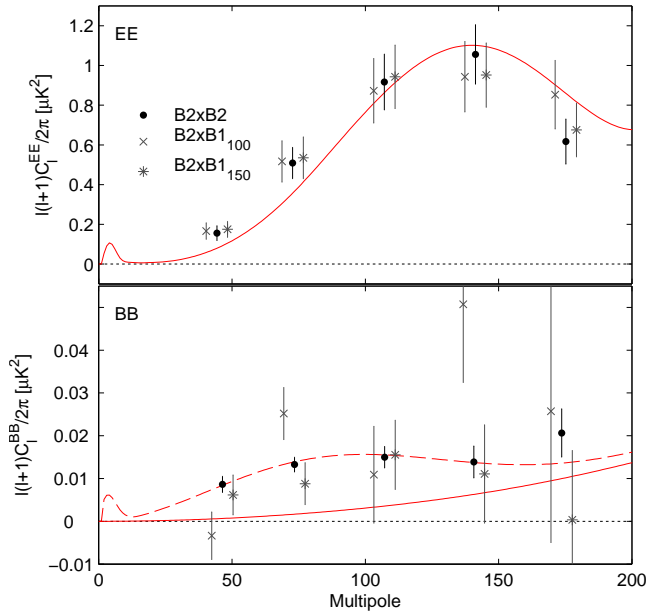


FIG. 7.— The BICEP2  $EE$  and  $BB$  auto spectra (as shown in Figure 2) compared to cross spectra between BICEP2 and the 100 and 150 GHz maps from BICEP1. The cross spectrum points are offset horizontally for clarity.

Pursuing this formally, we use simulations of both experiments observing a common sky to construct a combined likelihood function for bandpowers 1–5 of the BICEP2 auto, BICEP1<sub>100</sub> auto, and their cross spectrum using the Hamimeche & Lewis (2008) approximation; see B14 for implementation details. We use this likelihood function to fit a six-parameter model parametrized by the five 150 GHz bandpowers and a single common spectral index,  $\beta$ . Without loss of generality we take this spectral index to be the power law exponent of the signal’s antenna temperature as a function of frequency. We marginalize this six-parameter model over the bandpowers to obtain a one-parameter likelihood function over the spectral index.

Figure 8 shows the resulting estimate of the spectral index, with approximate  $1\sigma$  uncertainty range. We evaluate the consistency with specific values of  $\beta$  using a likelihood ratio test. The data are consistent with the spectrum of the CMB ( $\beta = -0.7$  for these bands and conventions), with a CMB-to-peak likelihood ratio of  $L = 0.68$ . Following Wilks (1938) we take  $\chi^2 \approx -2 \log L$  and evaluate the probability to exceed this value of  $\chi^2$  (for a single degree of freedom). A synchrotron spectrum with  $\beta = -3$  is disfavored ( $L = 0.076$ , PTE 0.023,  $2.3\sigma$ ), as is the preferred whole-sky dust spectrum from Planck Collaboration et al. (2013a), which corresponds under these conventions to  $\beta \approx +1.75$  ( $L = 0.091$ , PTE 0.028,  $2.2\sigma$ ). We have also conducted a series of simulations applying this procedure to simulated data sets with CMB and dust spectral indexes. These simulations indicate that the observed likelihood ratios are typical of a CMB spectral index but atypical of dust.

### 10.3. Additional Cross Spectra

Having seen that the BICEP2 auto spectrum is compatible with both the BICEP2×BICEP1<sub>100</sub> and the BICEP2×BICEP1<sub>150</sub> cross spectra we proceed to com-

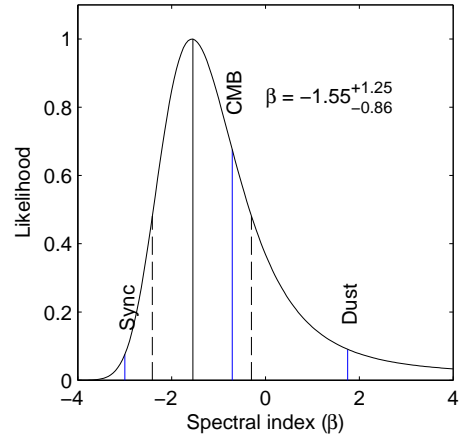


FIG. 8.— The constraint on the spectral index of the  $BB$  signal based on joint consideration of the BICEP2 auto, BICEP1<sub>100</sub> auto, and BICEP2×BICEP1<sub>100</sub> cross spectra. The curve shows the marginalized likelihood as a function of assumed spectral index. The vertical solid and dashed lines indicate the maximum likelihood and the  $\pm 1\sigma$  interval. The blue vertical lines indicate the equivalent spectral indices under these conventions for the CMB, synchrotron, and dust. The observed signal is consistent with a CMB spectrum, while synchrotron and dust are both disfavored by  $\gtrsim 2\sigma$ .

bine the latter<sup>36</sup>. Figure 9 compares the result to the BICEP2 auto spectrum from Figure 2. Taking the difference of these spectra and comparing to the differences of the lensed- $\Lambda$ CDM+noise+ $r = 0.2$  simulations the bandpower 1–5  $\chi^2$  and  $\chi$  PTEs are mid-range indicating compatibility.

Comparing the BICEP2×BICEP1<sub>comb</sub> spectrum to the lensed- $\Lambda$ CDM expectation the  $\chi^2$  and  $\chi$  values have PTE of 0.005 and 0.002 respectively corresponding to  $\approx 3\sigma$  evidence of excess power. The compatibility of the BICEP2 auto and BICEP2×BICEP1<sub>comb</sub> cross spectra combined with the detection of excess power in the cross spectra is powerful additional evidence against a systematic origin of the nominal signal given the significant differences in focal plane technology and beam imperfections.

The successor experiment to BICEP2 is the *Keck Array* which consists of five BICEP2 like receivers (Sheehy et al. 2010). The *Keck Array* data analysis is not yet complete and will be the subject of future publications. However as an additional systematics check we show in Figure 9 a cross spectrum between BICEP2 and preliminary *Keck Array* maps from the 2012 and 2013 seasons. This cross spectrum also shows obvious excess  $BB$  power at low  $\ell$ .

## 11. COSMOLOGICAL PARAMETER CONSTRAINTS

We have shown that our observed  $B$ -mode spectrum i) cannot be explained by systematics (jackknives, beam-map simulations, other systematics studies, and cross spectra with BICEP1<sub>150</sub>), and ii) seems highly unlikely to be dominated by foregrounds (dust model projections, dust model cross correlations, and spectral index constraints from cross spectra with BICEP1<sub>100</sub>). In this section we do some basic fitting of cosmological parameters while noting again that all the bandpowers and ancillary data are available for download so that others may conduct fuller studies.

### 11.1. Lensed- $\Lambda$ CDM + Tensors

<sup>36</sup> We combine using weights which minimize the variance of the lensed- $\Lambda$ CDM+noise simulations as described in B14.

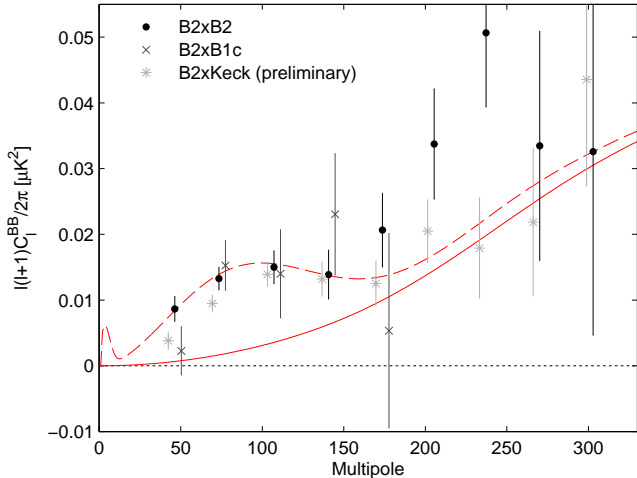


FIG. 9.— Comparison of the BICEP2  $BB$  auto spectrum and cross spectra taken between BICEP2 and BICEP1 combined, and BICEP2 and *Keck Array* preliminary. (For clarity the cross spectrum points are offset horizontally and the BICEP2  $\times$  BICEP1 points are omitted at  $\ell > 200$ .)

In Figure 2 we see a substantial excess of  $BB$  power in the region where an inflationary gravitational wave (IGW) signal would be expected to peak. We therefore proceed to find the most likely value of the tensor-to-scalar ratio  $r$  using the “direct likelihood” method introduced in B14. We first form additional sets of simulations for many values of  $r$  by combining the lensed- $\Lambda$ CDM and scaled  $r = 0.2$  simulations<sup>37</sup>. We then combine the bandpowers of these and the real bandpowers with  $s/n$  weighting where  $s$  is the IGW spectrum for a small value of  $r$  and  $n$  is the variance of the lensed- $\Lambda$ CDM+noise simulations. Arranging the simulation pdf values as rows we can then read off the likelihood curve for  $r$  as the columns at the observed combined bandpower value.

The result of this process is shown in Figure 10. Defining the confidence interval as the equal likelihood contour which contains 68% of the total likelihood we find  $r = 0.20^{+0.07}_{-0.05}$ . This uncertainty is driven by the sample variance in our patch of sky, and the likelihood falls off very steeply towards  $r = 0$ . The likelihood ratio between  $r = 0$  and the maximum is  $2.9 \times 10^{-11}$  equivalent to a PTE of  $3.3 \times 10^{-12}$  or  $7.0\sigma$ . The numbers quoted above are for bins 1–5 although due to the weighting step they are highly insensitive to this choice. (Absolute calibration and beam uncertainty are included in these calculations but have a negligible effect.)

Evaluating our simple  $\chi^2$  statistic between bandpowers 1–5 and the lensed- $\Lambda$ CDM+noise+ $r = 0.2$  simulations yields a value of 1.1, which for 4 degrees of freedom has a PTE of 0.90. The model is therefore a perfectly acceptable fit to the data.

In Figure 11 we recompute the  $r$  constraint subtracting each of the foreground models shown in Figure 6. For the auto spectra the range of maximum likelihood  $r$  values is 0.12–0.19, while for the cross it is 0.16–0.21 (random fluctuations in the cross can cause shifts up as well as down). The probability that each of these models reflects reality is hard to assess. Presumably greatest weight should be given to the DDM2 cross spectrum and we note that in this case the maximum likelihood value shifts down to  $r = 0.16^{+0.06}_{-0.05}$  with a like-

<sup>37</sup> Hence we assume always  $n_t = 0$  making the value of  $r$  independent of the pivot scale.

likelihood ratio between  $r = 0$  and maximum of  $2.2 \times 10^{-8}$ , equivalent to a PTE of  $2.9 \times 10^{-9}$  or  $5.9\sigma$ . Performing this subtraction slightly increases  $\chi^2$  (to 1.46) but the fit remains perfectly acceptable (PTE 0.84).

The dust foreground is expected to have a power law spectrum which slopes modestly down  $\propto \ell^{-0.6}$  in the usual  $l(l+1)C_l/2\pi$  units (Dunkley et al. 2009). In Figure 6 we see that the DDM2 model appears to do this in both auto and cross, before the auto spectrum starts to rise again due to noise in the polarization fraction and angle input maps. We note that the  $s/n$  bandpower weighting scheme described above weights the first bin very highly. Therefore if we were to exclude it the difference between the unsubtracted and foreground subtracted model lines in Figure 11 would be much smaller; i.e. while dust may contribute significantly to our first bandpower it definitely cannot explain bandpowers two through five.

Computing an  $r$  constraint using the BICEP2  $\times$  BICEP1<sub>comb</sub> cross spectrum shown in Figure 9 yields  $r = 0.19^{+0.11}_{-0.08}$ . The likelihood ratio between  $r = 0$  and the maximum is  $2.0 \times 10^{-3}$  equivalent to a PTE of  $4.2 \times 10^{-4}$  or  $3.5\sigma$ .

### 11.2. Scaled-lensing + Tensors

Lensing deflections of the CMB photons as they travel from last scattering re-map the patterns slightly. In temperature this leads to a slight smoothing of the acoustic peaks, while in polarization a small  $B$ -mode is introduced with a spectrum similar to a smoothed version of the  $EE$  spectrum a factor  $\sim 100$  lower in power. Using their own and other data Planck Collaboration XVI (2013) quote a limit on the amplitude of the lensing effect versus the  $\Lambda$ CDM expectation of  $A_L = 0.99 \pm 0.05$ .

Figure 12 shows a joint constraint on the tensor-to-scalar ratio  $r$  and the lensing scale factor  $A_L$  using our  $BB$  bandpowers 1–5. As expected there is an anti-correlation — one can partially explain the low  $\ell$  excess by scaling up the lensing signal. However, since the lensing and IGW signals have different spectral shapes the degeneracy is not complete. The maximum likelihood scaling is  $\approx 1.5$ . Marginalizing over  $r$  the likelihood ratio between peak and unity is 0.75 indicating compatibility, while the likelihood ratio between peak and zero is 0.03, equivalent to a PTE of  $7.0 \times 10^{-3}$  or a  $2.7\sigma$  detection of lensing in the BICEP2  $BB$  auto spectrum.

### 11.3. Compatibility with Temperature Data

If present at last-scattering, tensor modes will add power to all spectra including  $TT$ . For an  $r$  value of 0.2 the contribution to  $TT$  at the largest angular scales ( $\ell < 10$ ) would be  $\approx 10\%$  of the level measured by WMAP and *Planck*. The theoretical  $\Lambda$ CDM power level expected at these scales is dependent on several cosmological parameters including the spectral index of the initial scalar perturbations,  $n_s$ , and the optical depth to the last scattering surface,  $\tau$ . However by combining temperature data taken over a wide range of angular scales indirect limits on  $r$  have been set. Using WMAP+SPT data Story et al. (2013) quote  $r < 0.18$  (95% confidence) tightening to  $r < 0.11$  when also including measurements of the Hubble constant and baryon acoustic oscillations (BAO). More recently Planck Collaboration XVI (2013) quote  $r < 0.11$  using a combination of *Planck*, SPT and ACT temperature data, plus WMAP polarization (to constrain  $\tau$ ).

These limits appear to be in moderately strong tension with interpretation of our  $B$ -mode measurements as tensors. Since we have dispensed with the possibility of significant system-

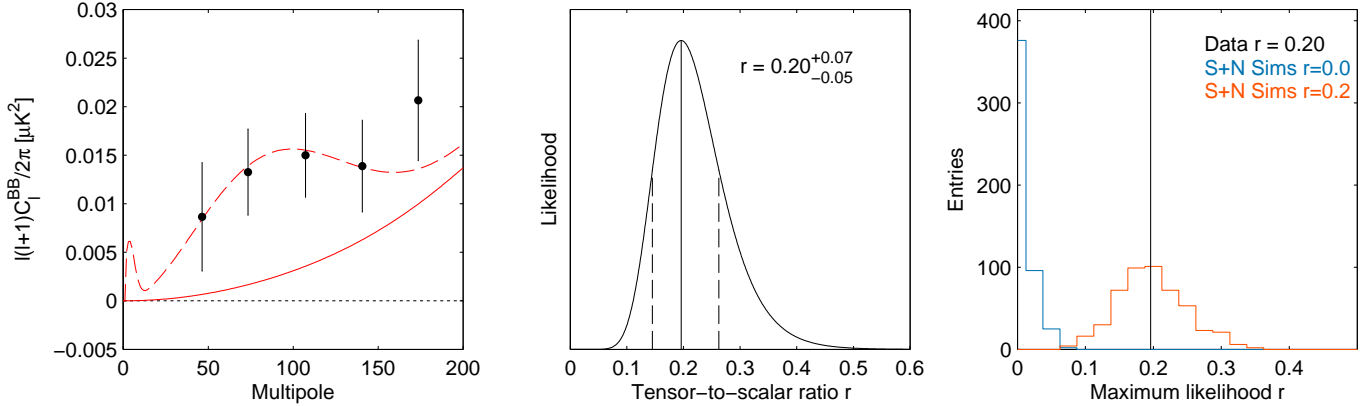


FIG. 10.— *Left*: The BICEP2 bandpowers plotted with the maximum likelihood lensed- $\Lambda$ CDM+ $r = 0.20$  model. The uncertainties are taken from that model and hence include sample variance on the  $r$  contribution. *Middle*: The constraint on the tensor-to-scalar ratio  $r$ . The maximum likelihood and  $\pm 1\sigma$  interval is  $r = 0.20^{+0.07}_{-0.05}$ , as indicated by the vertical lines. *Right*: Histograms of the maximum likelihood values of  $r$  derived from lensed- $\Lambda$ CDM+noise simulations with  $r = 0$  (blue) and adding  $r = 0.2$  (red). The maximum likelihood value of  $r$  for the real data is shown by the vertical line.

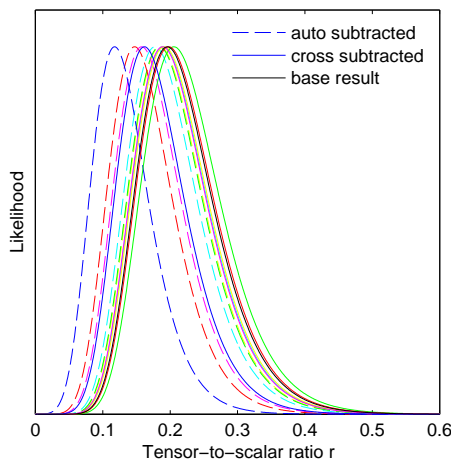


FIG. 11.— Modified constraints on the tensor-to-scalar ratio  $r$  when subtracting each of the foreground models shown in Figure 6 from the BICEP2  $BB$  bandpowers. The line styles and colors match Figure 6 with dashed for auto spectra and solid for cross spectra. The probability that each of these models reflects reality is hard to assess — see the text for discussion.

atic contamination, and shown that foreground is highly unlikely to contribute a large fraction of our observed signal, we must ask what extensions to the standard model might resolve this situation.

One obvious modification is to allow the initial scalar perturbation spectrum to depart from the simple power law form which is assumed in the base  $\Lambda$ CDM model. A standard way in which this is done is by introducing a “running” parameter  $dn_s/d\ln k$ . In Planck Collaboration XVI (2013) the constraint relaxes to  $r < 0.26$  (95% confidence) when running is allowed with  $dn_s/d\ln k = -0.022 \pm 0.010$  (68%) (for the *Planck*+WP+highL data combination). In Figure 13 we show the constraint contours when allowing running as taken from Figure 23 of Planck Collaboration XVI (2013), and how these change when the BICEP2 data are added. The red contours on the plot are simply the Monte Carlo Markov Chains (MCMC) (Gelman & Lopes 2006; Lewis & Bridle 2002) provided with the *Planck* data release<sup>38</sup> (and are thus identical to those shown in that *Planck* paper). We then apply

<sup>38</sup> As downloaded from <http://www.sciops.esa.int/>

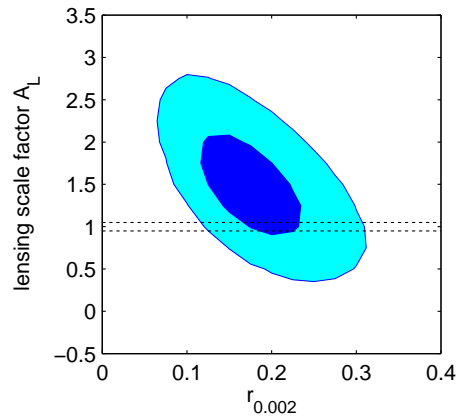


FIG. 12.— Joint constraints on the tensor-to-scalar ratio  $r$  and the lensing scale factor  $A_L$  using the BICEP2  $BB$  bandpowers 1–5. One and two  $\sigma$  contours are shown. The horizontal dotted lines show the  $1\sigma$  constraint from Planck Collaboration XVI (2013). The BICEP2 data are compatible with the expected amplitude of the lensing  $B$ -mode which is detected at  $2.7\sigma$ .

importance sampling (Hastings 1970) to these chains using our  $r$  likelihood as shown in Figure 10 to derive the blue contours, for which the running parameter constraint shifts to  $dn_s/d\ln k = -0.028 \pm 0.009$  (68%).

The point of Figure 13 is not to endorse running as the correct explanation of the observed deficit of low  $\ell$   $TT$  power. It is simply to illustrate one example of a simple model extension beyond standard  $\Lambda$ CDM+*tensors* which can resolve the apparent tension between previous  $TT$  measurements and the direct evidence for tensors provided by our  $B$ -mode measurements — probably there are others. Of course one might also speculate that the tension could be reduced within the standard  $\Lambda$ CDM+*tensors* model, for example if  $\tau$  or other parameters were allowed to shift. We anticipate a broad range of possibilities will be explored.

## 12. CONCLUSIONS

We have described the observations, data reduction, simulation and power spectrum analysis of all three seasons of data taken by the BICEP2 experiment. The polarization maps presented here are the deepest ever made at degree angular

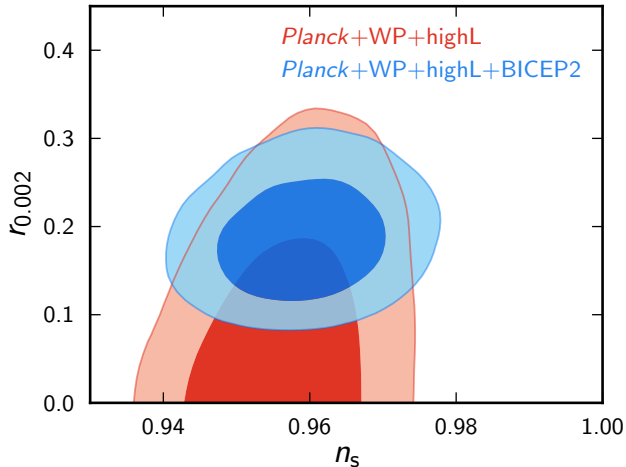


FIG. 13.— Indirect constraints on  $r$  from CMB temperature spectrum measurements relax in the context of various model extensions. Shown here is one example, following Planck Collaboration XVI (2013) Figure 23, where tensors and running of the scalar spectral index are added to the base  $\Lambda$ CDM model. The contours show the resulting 68% and 95% confidence regions for  $r$  and the scalar spectral index  $n_s$ , when also allowing running. The red contours are for the “Planck+WP+highL” data combination, which for this model extension gives a 95% bound  $r < 0.26$  (Planck Collaboration XVI 2013). The blue contours add the BICEP2 constraint on  $r$  shown in the center panel of Figure 10. See the text for further details.

scales having noise level of 87 nK-degrees in  $Q$  and  $U$  over an effective area of 380 square degrees.

To fully exploit this unprecedented sensitivity we have expanded our analysis pipeline in several ways. We have added an additional filtering of the timestream using a template temperature map (from *Planck*) to render the results insensitive to temperature to polarization leakage caused by leading order beam systematics. In addition we have implemented a map purification step that eliminates ambiguous modes prior to  $B$ -mode estimation. These deprojection and purification steps are both straightforward extensions of the kinds of linear filtering operations that are now common in CMB data analysis.

The power spectrum results are perfectly consistent with lensed- $\Lambda$ CDM with one striking exception: the detection of a large excess in the  $BB$  spectrum in exactly the  $\ell$  range where an inflationary gravitational wave signal is expected to peak. This excess represents a  $5.2\sigma$  excursion from the base lensed- $\Lambda$ CDM model. We have conducted a wide selection of jack-knife tests which indicate that the  $B$ -mode signal is common on the sky in all data subsets. These tests offer very strong empirical evidence against a systematic origin for the signal.

In addition we have conducted extensive simulations using high fidelity per channel beam maps. These confirm our understanding of the beam effects, and that after deprojection of the two leading order modes, the residual is far below the level of the signal which we observe.

Having demonstrated that the signal is real and “on the sky” we proceeded to investigate if it may be due to foreground contamination. Polarized synchrotron emission from our galaxy is easily ruled out using low frequency polarized maps from WMAP. For polarized dust emission public maps are not yet available. We therefore investigate a range of models including new ones which use all of the information which is currently available from *Planck*. These models all predict auto spectrum power well below our observed level. In addition none of them show any significant cross correlation with

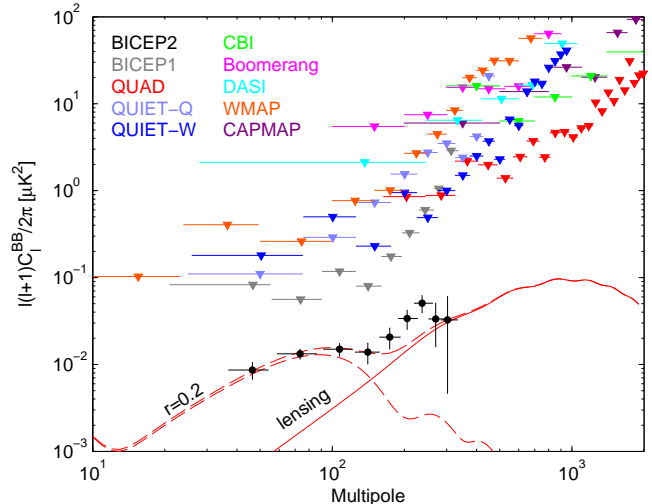


FIG. 14.— BICEP2  $BB$  auto spectra and 95% upper limits from several previous experiments (Leitch et al. 2005; Montroy et al. 2006; Sievers et al. 2007; Bischoff et al. 2008; Brown et al. 2009; QUIET Collaboration et al. 2011, 2012; Bennett et al. 2013; Barkats et al. 2014). The curves show the theory expectations for  $r = 0.2$  and lensed- $\Lambda$ CDM.

our maps.

Taking cross spectra against 100 GHz maps from BICEP1 we find significant correlation and set a constraint on the spectral index of the signal consistent with CMB, and disfavoring synchrotron and dust by  $2.3\sigma$  and  $2.2\sigma$  respectively. The fact that the BICEP1 and *Keck Array* maps cross correlate is powerful further evidence against systematics.

The simplest and most economical remaining interpretation of the  $B$ -mode signal which we have detected is that it is due to tensor modes — the IGW template is an excellent fit to the observed excess. We therefore proceed to set a constraint on the tensor-to-scalar ratio and find  $r = 0.20^{+0.07}_{-0.05}$  with  $r = 0$  ruled out at a significance of  $7.0\sigma$ . Multiple lines of evidence have been presented that foregrounds are a subdominant contribution: i) direct projection of the best available foreground models, ii) lack of strong cross correlation of those models against the observed sky pattern (Figure 6), iii) the frequency spectral index of the signal as constrained using BICEP1 data at 100 GHz (Figure 8), and iv) the spatial and power spectral form of the signal (Figures 3 and 10).

Subtracting the various dust models and re-deriving the  $r$  constraint still results in high significance of detection. For the model which is perhaps the most likely to be close to reality (DDM2 cross) the maximum likelihood value shifts to  $r = 0.16^{+0.06}_{-0.05}$  with  $r = 0$  disfavored at  $5.9\sigma$ . These high values of  $r$  are in apparent tension with previous indirect limits based on temperature measurements and we have discussed some possible resolutions including modifications of the initial scalar perturbation spectrum such as running. However we emphasize that we do not claim to know what the resolution is.

Figure 14 shows the BICEP2 results compared to previous upper limits. The long search for tensor  $B$ -modes is apparently over, and a new era of  $B$ -mode cosmology has begun.

BICEP2 was supported by the US National Science Foundation under grants ANT-0742818 and ANT-1044978 (Caltech/Harvard) and ANT-0742592 and ANT-1110087 (Chicago/Minnesota). The development of antenna-coupled detector technology was supported by the JPL Research and

Technology Development Fund and grants 06-ARPA206-0040 and 10-SAT10-0017 from the NASA APRA and SAT programs. The development and testing of focal planes were supported by the Gordon and Betty Moore Foundation at Caltech. Readout electronics were supported by a Canada Foundation for Innovation grant to UBC. The receiver development was supported in part by a grant from the W. M. Keck Foundation. The computations in this paper were run on the Odyssey cluster supported by the FAS Science Division Research Computing Group at Harvard University. Tireless ad-

ministrative support was provided by Irene Coyle and Kathy Deniston.

We thank the staff of the US Antarctic Program and in particular the South Pole Station without whose help this research would not have been possible. We thank all those who have contributed past efforts to the BICEP/Keck Array series of experiments, including the BICEP1 and Keck Array teams. We dedicate this paper to the memory of Andrew Lange, whom we sorely miss.

## REFERENCES

- Abbott, L. F., & Wise, M. B. 1984, *Nuclear Physics B*, 244, 541
- Albrecht, A., & Steinhardt, P. J. 1982, *Physical Review Letters*, 48, 1220
- Bardeen, J. M., Steinhardt, P. J., & Turner, M. S. 1983, *Phys. Rev. D*, 28, 679
- Barkats, D., Bischoff, C., Farese, P., et al. 2005, *Astrophys. J. Lett.*, 619, L127
- Barkats, D., Aikin, R., Bischoff, C., et al. 2014, *The Astrophysical Journal*, 783, 67
- Battye, R. A., Browne, I. W. A., Peel, M. W., Jackson, N. J., & Dickinson, C. 2011, *Mon. Not. Roy. Astron. Soc.*, 413, 132
- Bennett, C. L., Larson, D., Weiland, J. L., et al. 2013, *Astrophys. J. Suppl.*, 208, 20
- BICEP2 Collaboration II. 2014, Available on arxiv
- BICEP2 Collaboration III. 2014, In prep.
- Bischoff, C., Hyatt, L., McMahon, J. J., et al. 2008, *Astrophys. J.*, 684, 771
- Bock, J. J. 2003, in *Society of Photo-Optical Instrumentation Engineers (SPIE) Conference Series*, Vol. 4843, *Polarimetry in Astronomy*, ed. S. Fineschi, 314–323
- Brout, R., Englert, F., & Gunzig, E. 1978, *Annals of Physics*, 115, 78
- Brown, M. L., Ade, P., Bock, J., et al. 2009, *Astrophys. J.*, 705, 978
- Bunn, E. F., Zaldarriaga, M., Tegmark, M., & de Oliveira-Costa, A. 2003, *Phys. Rev. D*, 67, 023501
- Chiang, H. C., Ade, P. A. R., Barkats, D., et al. 2010, *Astrophys. J.*, 711, 1123
- Das, S., Louis, T., Nolta, M. R., et al. 2013, ArXiv e-prints, arXiv:1301.1037
- Delabrouille, J., Betoule, M., Melin, J.-B., et al. 2013, *Astr. & Astroph.*, 553, A96
- Dunkley, J., Amblard, A., Baccigalupi, C., et al. 2009, in *American Institute of Physics Conference Series*, Vol. 1141, *American Institute of Physics Conference Series*, ed. S. Dodelson, D. Baumann, A. Cooray, J. Dunkley, A. Fraisse, M. G. Jackson, A. Kogut, L. Krauss, M. Zaldarriaga, & K. Smith, 222–264
- Eimer, J. R., Bennett, C. L., Chuss, D. T., et al. 2012, in *Society of Photo-Optical Instrumentation Engineers (SPIE) Conference Series*, Vol. 8452, *Society of Photo-Optical Instrumentation Engineers (SPIE) Conference Series*
- Fabbri, R., & Pollock, M. D. 1983, *Physics Letters B*, 125, 445
- Finkbeiner, D. P., Davis, M., & Schlegel, D. J. 1999, *Astrophys. J.*, 524, 867
- Fraisse, A. A., Ade, P. A. R., Amiri, M., et al. 2013, *Journal of Cosmology and Astroparticle Physics*, 4, 47
- Gamerman, D., & Lopes, H. F. 2006, *Markov Chain Monte Carlo: Stochastic Simulation for Bayesian Inference (Chapman and Hall/CRC)*
- Górski, K. M., Hivon, E., Banday, A. J., et al. 2005, *Astrophys. J.*, 622, 759
- Grishchuk, L. P. 1975, *Soviet Journal of Experimental and Theoretical Physics*, 40, 409
- Guth, A. H. 1981, *Phys. Rev. D*, 23, 347
- Guth, A. H., & Pi, S.-Y. 1982, *Physical Review Letters*, 49, 1110
- Hamimeche, S., & Lewis, A. 2008, *Phys. Rev. D*, 77, 103013
- Hanson, D., Hoover, S., Crites, A., et al. 2013, *Physical Review Letters*, 111, 141301
- Hastings, W. 1970, *Biometrika*, 57, 97
- Hawking, S. W. 1982, *Physics Letters B*, 115, 295
- Hileman, T. E., Appel, J. W., Beal, J. A., et al. 2009, *AIP Conference Proceedings*, 1185
- Hinshaw, G., Larson, D., Komatsu, E., et al. 2013, *Astrophys. J. Suppl.*, 208, 19
- Hivon, E., Górski, K. M., Netterfield, C. B., et al. 2002, *Astrophys. J.*, 567, 2
- Hou, Z., Reichardt, C. L., Story, K. T., et al. 2014, *Astrophys. J.*, 782, 74
- Irwin, K. D. 1995, *Applied Physics Letters*, 66, 1998
- Kamionkowski, M., Kosowsky, A., & Stebbins, A. 1997, *Physical Review Letters*, 78, 2058
- Kaufman, J. P., Miller, N. J., Shimon, M., et al. 2013, ArXiv e-prints, arXiv:1312.7877
- Kazanas, D. 1980, *Astrophys. J. Lett.*, 241, L59
- Keating, B. G., Ade, P. A. R., Bock, J. J., et al. 2003, in *Society of Photo-Optical Instrumentation Engineers (SPIE) Conference Series*, Vol. 4843, *Polarimetry in Astronomy*, ed. S. Fineschi, 284–295
- Keating, B. G., Shimon, M., & Yadav, A. P. S. 2013, *Astrophys. J. Lett.*, 762, L23
- Knox, L. 1999, *Phys. Rev. D*, 60, 103516
- Kogut, A., Ade, P. A. R., Benford, D., et al. 2012, in *Society of Photo-Optical Instrumentation Engineers (SPIE) Conference Series*, Vol. 8452, *Society of Photo-Optical Instrumentation Engineers (SPIE) Conference Series*
- Kovac, J. M., Leitch, E. M., Pryke, C., et al. 2002, *Nature*, 420, 772
- Krauss, M., & Wilczek, F. 2013, ArXiv e-prints, arXiv:1309.5343
- Leitch, E. M., Kovac, J. M., Halverson, N. W., et al. 2005, *Astrophys. J.*, 624, 10
- Lewis, A. 2011, *LensPix: Fast MPI full sky transforms for HEALPix*, astrophysics Source Code Library, ascl:1102.025
- Lewis, A., & Bridle, S. 2002, *Phys. Rev. D*, 66, 103511
- Linde, A. D. 1982, *Physics Letters B*, 108, 389
- . 1983, *Physics Letters B*, 129, 177
- Massardi, M., Ekers, R. D., Murphy, T., et al. 2011, *Mon. Not. Roy. Astron. Soc.*, 412, 318
- Montroy, T. E., Ade, P. A. R., Bock, J. J., et al. 2006, *Astrophys. J.*, 647, 813
- Mukhanov, V. F. 1985, *ZhETF Pisma Redaktsiiu*, 41, 402
- Mukhanov, V. F., & Chibisov, G. V. 1981, *Soviet Journal of Experimental and Theoretical Physics Letters*, 33, 532
- Niemack, M. D., Ade, P. A. R., Aguirre, J., et al. 2010, in *Society of Photo-Optical Instrumentation Engineers (SPIE) Conference Series*, Vol. 7741, *Society of Photo-Optical Instrumentation Engineers (SPIE) Conference Series*
- O’Dea, D. T., Clark, C. N., Contaldi, C. R., & MacTavish, C. J. 2012, *Mon. Not. Roy. Astron. Soc.*, 419, 1795
- Page, L., Hinshaw, G., Komatsu, E., et al. 2007, *Astrophys. J. Suppl.*, 170, 335
- Peiris, H. V., Komatsu, E., Verde, L., et al. 2003, *Astrophys. J. Suppl.*, 148, 213
- Penzias, A. A., & Wilson, R. W. 1965, *Astrophys. J.*, 142, 419
- Planck Collaboration, Abergel, A., Ade, P. A. R., et al. 2013a, ArXiv e-prints, arXiv:1312.1300
- Planck Collaboration, Ade, P. A. R., Aghanim, N., et al. 2013b, ArXiv e-prints, arXiv:1303.5088
- Planck Collaboration XV. 2013, ArXiv e-prints, arXiv:1303.5075
- Planck Collaboration XVI. 2013, ArXiv e-prints, arXiv:1303.5076
- Planck Collaboration XXII. 2013, ArXiv e-prints, arXiv:1303.5082
- POLARBEAR Collaboration, Ade, P. A. R., Akiba, Y., et al. 2013a, ArXiv e-prints, arXiv:1312.6645
- . 2013b, ArXiv e-prints, arXiv:1312.6646
- . 2014, ArXiv e-prints, arXiv:1403.2369
- Polnarev, A. G. 1985, *Sov. Ast.*, 29, 607
- Pryke, C., Ade, P., Bock, J., et al. 2009, *Astrophys. J.*, 692, 1247
- QUIET Collaboration, Bischoff, C., Brizius, A., et al. 2011, *Astrophys. J.*, 741, 111
- QUIET Collaboration, Araujo, D., Bischoff, C., et al. 2012, *Astrophys. J.*, 760, 145
- Readhead, A. C. S., Myers, S. T., Pearson, T. J., et al. 2004, *Science*, 306, 836
- Reichborn-Kjennerud, B., Aboobaker, A. M., Ade, P., et al. 2010, in *Society of Photo-Optical Instrumentation Engineers (SPIE) Conference Series*, Vol. 7741, *Society of Photo-Optical Instrumentation Engineers (SPIE) Conference Series*
- Rubakov, V. A., Sazhin, M. V., & Veryaskin, A. V. 1982, *Physics Letters B*, 115, 189

- Sato, K. 1981, *Mon. Not. Roy. Astron. Soc.*, 195, 467
- Seljak, U. 1997, *Astrophys. J.*, 482, 6
- Seljak, U., & Zaldarriaga, M. 1997, *Physical Review Letters*, 78, 2054
- Sheehy, C. D. 2013, Progress toward a detection of inflationary B-modes with the BICEP2 and Keck Array polarimeters, copyright - Copyright ProQuest, UMI Dissertations Publishing 2013; Last updated - 2014-02-11; First page - n/a; M3: Ph.D.
- Sheehy, C. D., et al. 2010, Millimeter, Submillimeter, and Far-Infrared Detectors and Instrumentation for Astronomy V, 7741, 77411G
- Shimon, M., Keating, B., Ponthieu, N., & Hivon, E. 2008, *Phys. Rev. D*, 77, 083003
- Sievers, J. L., Achermann, C., Bond, J. R., et al. 2007, *Astrophys. J.*, 660, 976
- Sievers, J. L., Hlozek, R. A., Nolta, M. R., et al. 2013, *Journal of Cosmology and Astroparticle Physics*, 10, 60
- Smith, K. M. 2006, *Phys. Rev. D*, 74, 083002
- Spergel, D. N., & Zaldarriaga, M. 1997, *Physical Review Letters*, 79, 2180
- Starobinsky, A. A. 1979, *ZhETF Pisma Redaktsiiu*, 30, 719
- . 1980, *Physics Letters B*, 91, 99
- . 1982, *Physics Letters B*, 117, 175
- Story, K. T., Reichardt, C. L., Hou, Z., et al. 2013, *Astrophys. J.*, 779, 86
- Takahashi, Y. D., Ade, P. A. R., Barkats, D., et al. 2010, *Astrophys. J.*, 711, 1141
- Tegmark, M., & de Oliveira-Costa, A. 2001, *Phys. Rev. D*, 64, 063001
- van Engelen, A., Keisler, R., Zahn, O., et al. 2012, *Astrophys. J.*, 756, 142
- Wilks, S. S. 1938, *The Annals of Mathematical Statistics*, 9, 60
- Wu, J. H. P., Zuntz, J., Abroe, M. E., et al. 2007, *Astrophys. J.*, 665, 55